Mechanical Engineering Master Thesis

Giacomo Quattrucci

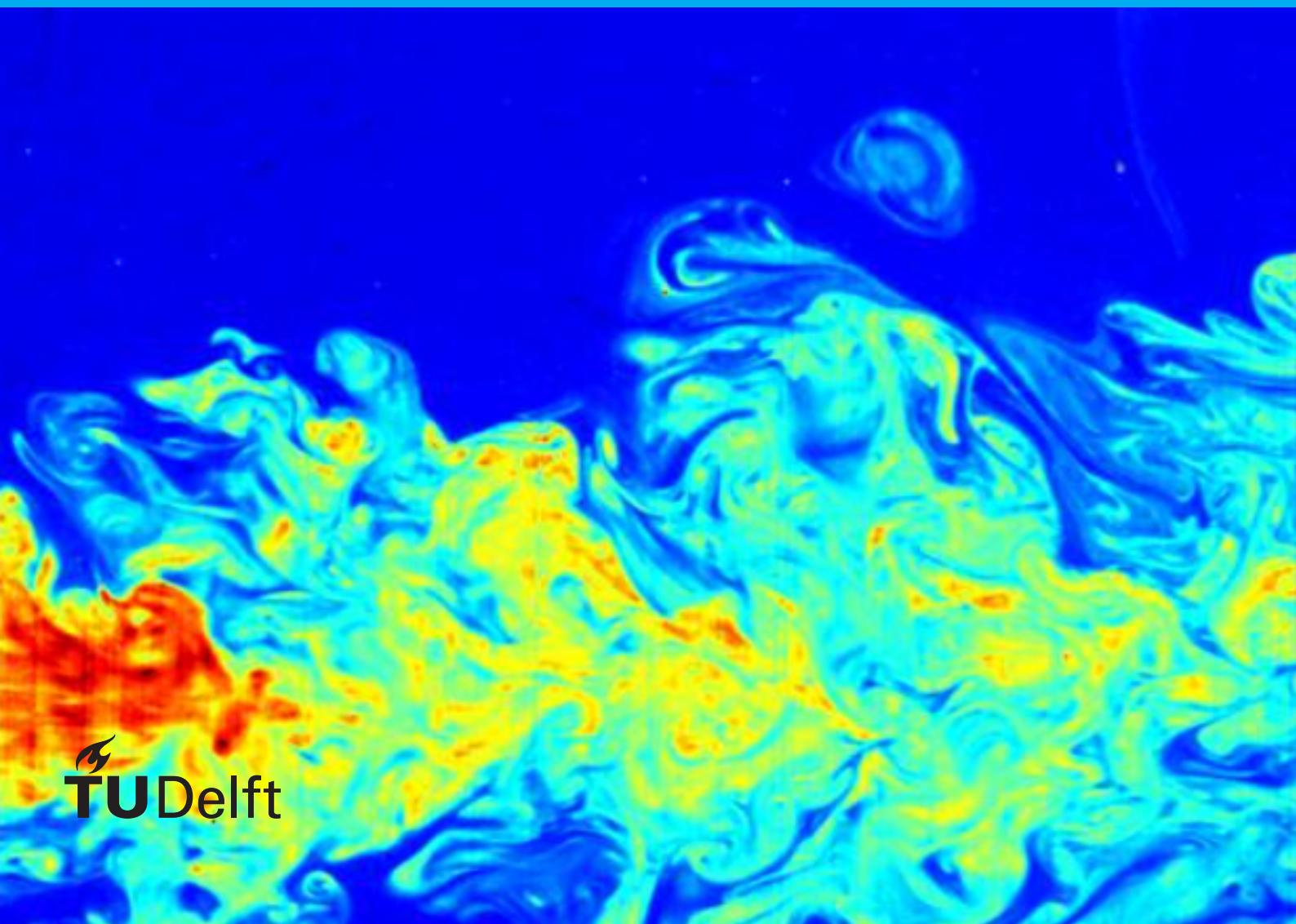

TU Delft

MASTER THESIS

Numerical study of heat transfer and buoyancy effects in mixed convective turbulent pipe flow

Programme: MsC in Mechanical Engineering
Track: Energy and Process Technology

Author: Giacomo Quattruci
Student ID: 4820428

Supervisor: Dr.ir. Jurriaan Peeters

Delft, April 22^{nd} 2022

Abstract

The optimization of heat transfer in turbulent upward pipe flows is a very common problem in engineering, due to the wide range of applications. However, this set-up is usually categorised as mixed convection flow, which means that gravity plays an important role. Sometimes, it might lead to heat transfer deterioration.
This research will simulated three different physical flow conditions gained by Shehata et Al. [3]: turbulent, sub-turbulent and laminarizing. The model will be constructed with OpenFOAM using two different approaches: RANS and LES. The former is applied to a two-dimensional geometry, whereas the latter is employed for a 3D cylinder mesh. For both of them air physical properties are implemented as function of temperature and the Boussinesq approximation is selected to forecast density variations.
Results is an assessment of RANS and LES differences and which one is more accurate, comparing normalized temperatures at axial locations to real experimental data. In the end, the role of gravity is studied, showing laminarization and using the sub-turbulent case to demonstrate how the presence or the absence of buoyancy forces influences heat transfer.

Acknowledgments

First of all, I would like to thank my supervisor, Dr.ir. Jurriaan W. R. Peeters for sharing his professional experience for the entire project. His trust and suggestions not only have widen my knowledge as a professional but also changed my mindset as an individual.
I would like to thank the committee for spending valuable time to read and participate to my thesis defence.
Lastly, I am deeply glad to have always received unconditional love from my family, who never doubt my ambitions or let me down in difficult periods. Thanks to all my friends spread around the world, who supported me even if separated by long distances or by a global pandemic.

Contents

List of Figures

List of Tables

1

Introduction

The following sub-sections will give a brief background about the importance of the simulated set-ups though its practical applications in the industrial field. Furthermore, some of the physical and computational problems related to the design process are going to be listed. Finally, the chapter is concluded describing the main goals of this research.

1.1. Heat Transfer

Heat transfer is the key phenomena for the majority of engineering applications. However, in today's society one of the main concerns is to reduce environmental impacts, using alternative or conventional working fluids [18]. Furthermore, efficient processes are the best solution for a reductions energy-intensive and expensive methods [19].
Specifically heated pipes have gained the attentions of research community, because of its technology advances [20] and the variety of suitable implementations. These set-ups are usually characterised by the so-called turbulent mixed convection flows.

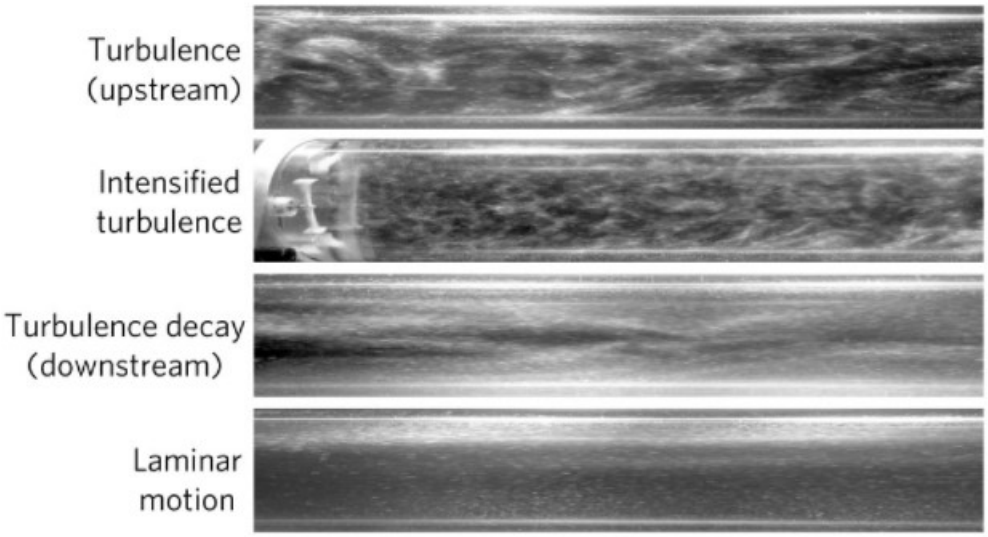

Figure 1.1: Experiment with different types of pipe flows. From top to bottom: entrance turbulent flow, intensified turbulent flow through a propeller, drop of turbulence moving downstream and complete laminarization. Source: [39]

These are turbulent flows that combine forced and natural convection, which are found in many engineering fields like: electronic devices cooling systems, nuclear reactors, gas-cooled reactors [12], super-critical water-cooled reactors [74], chemical processes [69], energy production [73] and rocket propulsion systems [72].

Turbulence is an advantageous mean for heat transfer, in contrast to a flow becoming laminar, which deteriorates the convection rate. It is possible to see this physical phenomena in Fig. 1.1, where buoyancy modifies the velocity field, destroying turbulence structure and consequently laminarizing the flow.
The first who find out about this problem, believed it was strictly connected to the super-critical flows [58] [4], then scientists realised was a matter of buoyancy and not of state of matter [13] [59].
This has become an obstacle for the scientific research, because it is hard to quantify and to forecast. However, This is the reason why the current study will try to analyse the this physical behaviour, using OpenFOAM.

1.2. Research objectives

This research analyses the heat transfer behaviour of three different flows: turbulent, sub-turbulent and laminarizing. These characterize a vertical heated pipe, where mixed convection occurs. Since researches about this topic are still rare, it might be important to gain more information witch more affordable and time efficient methods as performing CFD simulations. The current study searches an answer for the following questions:

1. Does a 2D RANS simulation properly approximate a mixed convection turbulent pipe flow?
2. How accurate is a 3D LES simulation, comparing it with real experimental data?
3. What are the main consequences of buoyancy concerning heat transfer?

2

Physics

This chapter is divided into four sections: the buoyancy contribution to flow characteristics, laminarization, turbulence and Boussinesq approximation. These are all physical phenomena and mathematical expressions that have been an influence for building the simulation and for the results analysis.

2.1. Buoyancy Contribution

In general, three different types of convection can be identified based on the action of gravity generating buoyancy forces. Its magnitude and relationship with pressure or external forces in the flow field characterizes convection heat transfer, which can be divided in following main categories:

1. ***Forced Convection***: The heat transfer is a result of the external force acting on the fluid (i.e. a pressure gradient created by a pump), which commonly creates a thermal boundary layer [48].
2. ***Mixed Convection***: The heat transfer is guided by pressure forces in a flow where density perturbations occurs non-uniformly, which implies that gravitational forces cannot be neglected [40].
3. ***Natural Convection***: The heat transfer is lead exclusively by strong density variations, which in turns generate buoyancy forces that lead to fluid motion [48].

Usually, the Richardson number is used to determine at which convection category the analysed flow belongs to [47]:

$$Ri = \frac{g\beta\Delta TL}{u^2} \tag{2.1}$$

$$\begin{cases} \text{Ri} < 0.1 \implies \textit{Forced Convection} \\ 0.1 < \text{Ri} < 10 \implies \textit{Mixed Convection} \\ \text{Ri} > 10 \implies \textit{Natural Convection} \end{cases} \tag{2.2}$$

g is the gravitational acceleration, β is the thermal expansion coefficient, ΔT is the temperature difference between the hot and reference one, L is the characteristic length and u is the velocity. Using the definition of the dimensionless Reynolds (Re) and Grashof numbers (Gr), Ri can be re-written as:

$$\begin{cases} Re = \frac{\rho uL}{\mu} \\ \\ Gr = \frac{g\beta\Delta TL^3}{\nu^2} \end{cases} \implies Ri = \frac{Gr}{Re^2} \tag{2.3}$$

μ and ν corresponds to dynamic and kinematic viscosity, respectively.Eq. 2.3 holds only if the free-fall velocity is used.
Thus, it cannot be applied for mixed convection, instead Buoyancy number (Bu) is used. This non-dimensional parameter is a semi-empirical equation [40] that represents the Richardson number modified for this specific flows [8]:

$$Bu = \overline{Gr_b} / Re_b^{2.7} \tag{2.4}$$

where $\overline{Gr_b} = \rho_b(\rho_b - \overline{\rho})gD^3/\mu_b^2$ indicates the local Grashof number based on average density difference. The convection affects the heat transfer rate when $Bu > 10^{-5}$. This parameter will be used to explain laminarization in the next section.
In addition, the manner in which buoyancy affects turbulence matters on the direction of the flow, local heat transfer coefficients are increased or decreased depending on the physical system:

- ***Aided flows***: The buoyancy forces have equal sign of the forced flow velocity. Concerning pipes, this happens for heated upward flow or cooled downward flow [36].
- ***Opposed flows***: The buoyancy forces have opposite sign of the forced flow velocity. Concerning pipes, this happens for heated downward flow or cooled upward flow [36].

The next sub-section is going to explain that specifically for heated upward flow, the heat transfer properties might be lower or higher than forced convection flows [41]. Usually very large buoyancy forces enhances heat transfer, whereas moderate values drop the convection contribution.
Indeed, in the specific case of mixed convection flows, studies has revealed that in particular physical condition the flow transition from turbulent to laminar at a certain point in time. Consequently, heat transfer deteriorates due to turbulence drop.

2.2. Laminarization

Laminarization is a physical phenomena that links buoyancy and inertia effects [74], causing mountainous transformation from a chaotic turbulent to laminar flow. This issue was already faced in the late 60s [58] [4] while studying super-critical steam cycles. Researches have tried to formalise possible correlations between physical characteristics [61] to forecast laminarization.
However, more information were gained during the 90s when hydraulic resistance [65] and buoyancy effects [59] [21] were deeper analysed in vertical heated tubes, demonstrating that laminarization does not exclusively occur in critical state flow conditions.
Still nowadays, very few studies can be found this topic [56] [62] [45], even less about trying to model its analytical solutions [61] [54] [54]. None of them have delivered convincing generalised formulations [8] due to the local change of temperature profile, causing steep changes of thermo-physical properties.
Especially in vertical pipes, also the gravity component (generally defined as $\rho g_i u_i$) in the governing equations contributes to the turbulence structure and its physical parameters across the flow field. In fact as introduced in the section above, one of the laminarization consequences is the drop in the heat transfer coefficient.
This process is described with formation of a fluid layer at the wall, with lower values of eddy diffusivities in the turbulent flow core [65], where the coexistence of low turbulent shear stresses and radial velocity gradients are present together with the convective acceleration peak of the flow.
Notably, sharp changes in density affect turbulence production, because of the heated flow acceleration caused by the thermal exchange or due to the influences of buoyancy. These events combined with large variations of fluid properties have dramatic consequences on heat transfer effectiveness [37].

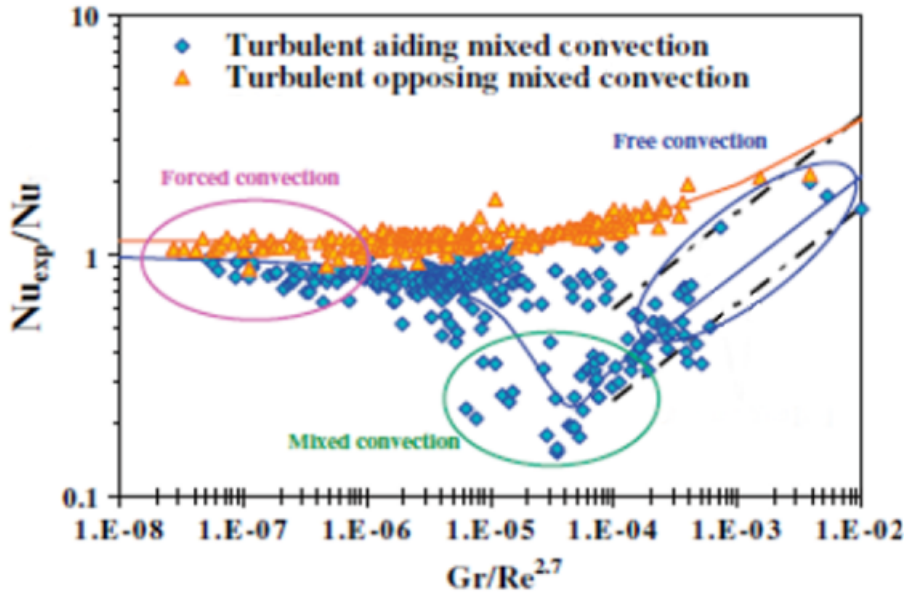

Figure 2.1: The Nusselt ratio between experimental and forced convection versus Buoyancy number at different flow conditions. Source: [2]

This is shown by Fig. 2.1, which correlates the Nusselt number ratios with Fewster's experiment [41] in circular pipes, divided by local Nusselt number calculated with Eq. 2.5 [40], versus the Buoyancy number.

$$Nu = 0.0183 Re_b^{0.82} Pr_b^{0.5} (\rho_w/\rho_b)^{0.3} (\overline{c_p}/c_{pb})^n \tag{2.5}$$

c_p is the specific heat capacity at constant pressure and n is temperature dependent exponent.
Considerable amount of experiments have shown that the Eq. 2.5, is the most agreeable with reality, as stated by [44].
Looking at Fig. 2.1, upward and downward flows are plotted, showing on the left side of the picture similar values in mixed convection in cooling conditions, where free convection predominates. Same conditions are given on the right side, hence for low values of Bu where forced convection guides the flow [8].
Fig. 2.1 demonstrates what stated in previously about mixed convection: heat transfer is enhanced in downward flows and deteriorated in upward flows.
This is a qualitatively and graphical confirmation that convective heat transfer coefficient drop due to the laminarization. This process is defined as heat transfer deterioration [5] [41].
In conclusion, new correlation for the Nusselt number constantly come out from scientific papers, but none of them has been able to give a good approximation, principally due to the laminarization which develops unexpectedly without a clear pattern of the Bu values.

2.3. Turbulence scale

Turbulence is a three-dimensional, unsteady physical process, which leads to chaotic motion at various scales. According to the Reynolds decomposition [42], turbulence can be described mathematically by defining physical variables as a sum of two components. For example, Eq. 2.6 is the generic flow velocity decomposition.

$$u = \overline{u} + u' \tag{2.6}$$

where $\overline{u}$ is the average contribution and u' is the perturbation [23].
In particular, u' represents random movement of fluid particles that creates rotating structures, usually referred as turbulent eddies [66]. The largest ones occurs far away from walls, lead by inertia effects with negligible viscosity. The large eddies are deformed, increasing the rotation and decreasing their radius. At the same time the stretching work also provides the energy which maintains the turbulence itself.
Thus, they break down in smaller eddies until they reach the Kalmurgorov scale [23]. There, they are dominated by viscosity until they are completely dissipated.

This downgrade progression in terms of eddies size is defined as energy cascade. Despite the properties perturbations can be approximated with fluctuating waves, also their characteristic energy will be a function of a wave. Indeed, the definition of spectral energy is the one contained in turbulent flow depending on frequencies variations. This is exactly what Fig. 2.2 is stating, using the Wave number ($\kappa = 2/\lambda$ with λ = eddies wave length) as a unit.

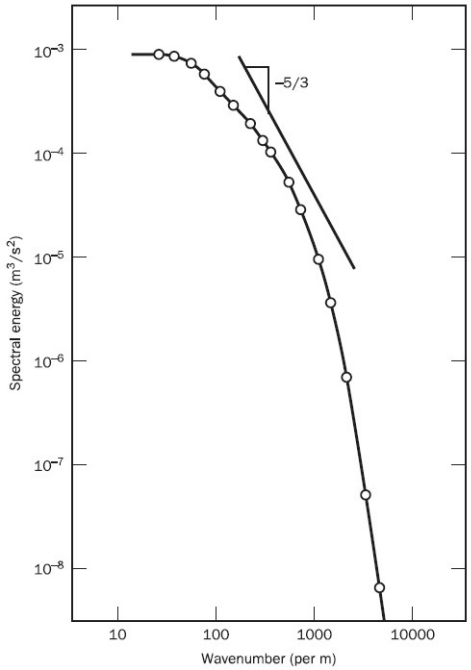

Figure 2.2: Energy spectrum versus the Wave number. Source: [66]

The diagram shows what it has been just explained: the energy reaches its peaks at the low κ (larger eddies), then it rapidly drop as soon as Wave number increases (small eddies). In addition, this figure will be recalled to illustrate and differentiate the computational fluid dynamics (CFD) models.

2.4. Fluid characteristic

In this research, the Boussinesq approximation is applied [11]. It delivers acceptable results when the variation of density is small, which implies a constant quantity, making an exception for the gravitational term ρg in the governing equations.
Therefore, mathematically the approximation can be traduced as a linear function of temperature times a coefficient of proportionality:

$$\rho \approx \rho_0[1 - \beta(T - T_0)] \tag{2.7}$$

β is the volumetric thermal expansion coefficient (already present in Gr definition), defined as:

$$\beta = \frac{1}{\rho}\left(\frac{\partial \rho}{\partial T}\right)_p \tag{2.8}$$

The subscript "p" next to the derivative indicates that the pressure is held constant [68].

3

Computational fluid dynamics theory

The main challenge in CFD simulations is to replicate turbulence with accuracy of mesh that must be necessarily fine to resolve all the length-scale while reducing the notorious characteristic of being time-consuming [55]. Fig. 3.1 illustrates the three main approaches used to resolve flow field by CFD software.

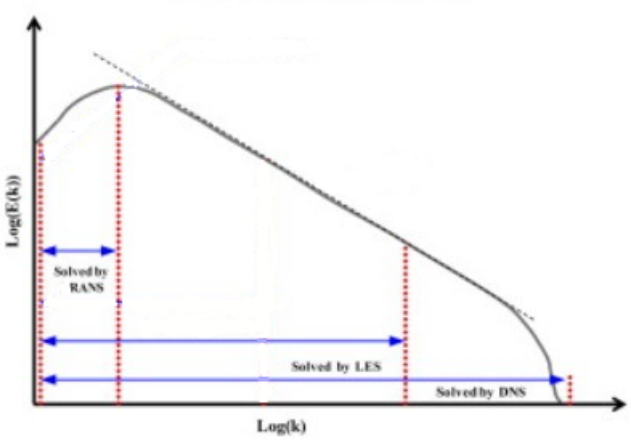

Figure 3.1: Example to avoid for building a regular mesh

Fig. 3.1 is the logarithmic plot of Fig. 2.2 and it distinguishes the three most used models for CFD: the Direct Numerical Simulation (DNS), the Large Eddy Simulation (LES) and Reynolds Average Navier-Stokes equations (RANS).
In this regard, DNS are usually accurate [75] [9], because it directly solves all the vortex scales, showing good agreement with experimental results [7]. However, DNS is a very expensive method, which can be shown with the following equation, that co-relates computational effort with the necessary iterations for a respectable output [23]:

$$NxM = O(Re^{11/4}) \tag{3.1}$$

with N indicating the total number of grid cells and M steps for the total number of integration steps. This is the reason why, RANS and LES were chosen for this research, as a potential good compromise between precision and time consumption.

3.1. RANS Models

Recalling Eq. 2.6, RANS methodology decomposes physical properties into mean and perturbation components. The mean part is averaged on time as Eq. 3.2

$$u = \overline{u} + u' \quad \text{with} \quad \overline{u} = \frac{1}{T}\int_{-\frac{1}{2}T}^{+\frac{1}{2}T} u(t+\tau)\, d\tau \tag{3.2}$$

T indicates the average time.
If this averaging is made for all the flow variables and inserted in the Navier-Stokes equations, a new term called the "Reynolds-stress tensor" appears. Since Boussinesq introduction of eddy viscosity [11] in 1877, the modelling of this tensor determine the differentiation between RANS solvers. Therefore RANS are traditionally classified in the following categories [6]:

- ***Zero-equation models:*** This model, also called mean-velocity field closures [24], just solves the system of equations using mixing length theory.
- ***One-equation models:*** This model introduce another equation to the system that must be solved. This is often the average kinetic energy calculation, which is used to find turbulence velocity scale. However, there are some exceptions like Spalart and Allmaras Model, which proposes a modified viscosity as added equation.
- ***Two-equation models:*** This model adds another physical properties compared to the one-equation one. The additional equation expresses the dissipation of the kinetic energy.

3.1.1. RANS Governing Equations

The Boussinesq approximation introduced before is now applied in Eq. 3.3, Eq. 3.4 and Eq. 3.5 to simplify the mathematical analysis. The standard Navier-Stokes equations for this case are:

Mass Equation:

$$\frac{\partial u_i}{\partial x_i} = 0 \tag{3.3}$$

Momentum Equation:

$$\frac{\partial u_i}{\partial t} + u_j\frac{\partial u_i}{\partial x_j} = -\frac{1}{\rho_0}\frac{\partial P}{\partial x_i} + \nu\frac{\partial^2 u_i}{\partial x_j x_j} - \beta\theta g \tag{3.4}$$

Energy Equation:

$$\frac{\partial \theta}{\partial t} + u_j\frac{\partial \theta}{\partial x_j} = \alpha\frac{\partial^2 \theta}{\partial x_j x_j} \tag{3.5}$$

where p is pressure and θ is temperature and ρ_0 is a constant reference density. Thus, applying Reynolds decomposing to the flow characteristic quantities in the above expressions ($u_i = \overline{u_i} + u_i'$, $p = \overline{p} + p'$ and $\theta = \overline{\theta} + \theta'$), the resulting averaged Navier-Stokes equations are:

$$\frac{\partial \overline{u_i}}{\partial x_i} = 0 \tag{3.6}$$

$$\frac{\partial \overline{u_i}}{\partial t} + \frac{\partial \overline{u_j u_i}}{\partial x_j} = -\frac{1}{\rho_0}\frac{\partial \overline{P}}{\partial x_i} + \nu\frac{\partial^2 \overline{u_i}}{\partial x_j x_j} - \frac{\partial \overline{u_i' u_j'}}{\partial x_j} - \beta\theta g \tag{3.7}$$

$$\frac{\partial \theta}{\partial t} + \frac{\partial \overline{u_j\theta}}{\partial x_j} = \alpha\frac{\partial^2 \theta}{\partial x_j x_j} - \frac{\partial \overline{u_i'\theta'}}{\partial x_j} \tag{3.8}$$

The additional diffusion terms are: Reynolds stresses ($u_i' u_j'$) in the momentum equation and Turbulent heat flux ($u_j'\theta'$) in the energy equation. These non-linear terms require specific conditions called turbulence closure problem, which defines the variety of solvers.

3.2. LES Models

LES models can be distinguished by RANS because they employ an avaraging based on space and not on time. These mathematical operation is commonly referred as filter, it is given by Eq. 3.9

$$[f(x_1,x_2,x_3)] = \iiint_{Volume} G(\underline{\xi}-\underline{x})f(\underline{x})\,d\xi_1\,d\xi_2\,d\xi_3 \tag{3.9}$$

Therefore, the Navier-Stokes equations solves large scales and approximates small ones depending on the filter function above annotated as $G(\underline{\xi}-\underline{x})$.

3.2.1. LES Governing Equations

Same considerations given previously for the RANS governing equations about Boussinesq approximation, are also used for LES ones. Therefore, the averaged Navier-Stokes equations are:

$$\frac{\partial[u_i]}{\partial x_i} = 0 \tag{3.10}$$

$$\frac{\partial[u_i]}{\partial t} + \frac{\partial[u_j][u_i]}{\partial x_j} = -\frac{1}{\rho_0}\frac{\partial[P]}{\partial x_i} + \nu\frac{\partial^2[u_i]}{\partial x_j x_j} - \frac{\partial[u_i' u_j']}{\partial x_j} - \beta\theta g \tag{3.11}$$

$$\frac{\partial[\theta]}{\partial t} + \frac{\partial[u_j][\theta]}{\partial x_j} = \alpha\frac{\partial^2[\theta]}{\partial x_j x_j} - \frac{\partial[u_i'\theta']}{\partial x_j} \tag{3.12}$$

These equations looks very similar to the RANS equations, except for the stress term in the momentum one, which in the LES model is usually referred as sub-grid stress (SGS). It describes the stress at micro-structure level, making it different to Reynolds stresses who is the mathematical expression of stresses at all scales on the average flow [23].

3.3. Closure Turbulence Modelling Problem

As briefly mentioned before, Boussinsesq has been the first defining the eddy-viscosity, which still today is the most used method to model Reynold stresses or SGS in case of LES simulations. According to this procedure, the eddy viscosity (ν_t) links turbulence stresses and the mean strain rate, playing the role of proportional coefficient [23].

$$\overline{u_i' u_j'} = -\nu_t\Big(\frac{\partial\overline{u_i}}{\partial x_j} + \frac{\partial\overline{u_i}}{\partial x_j}\Big) + \frac{2}{3}k\delta_{ij} \tag{3.13}$$

where k is the turbulent kinetic energy. Eq. 3.13 describes the case of a RANS; however, LES has the same term, except for the ν_{SGS} instead of ν_t.
Same process can be applied to introduce the eddy diffusivity (α_t) to model the turbulent heat flux as follows:

$$\overline{u_j'\theta'} = -\alpha_t\frac{\partial\overline{\theta}}{\partial x_i} \tag{3.14}$$

This approach is widely used even nowadays because it reduces the complexity of the closure problem, focusing the attention on giving a condition to ν_t and α_t.

4

Methodology

This section will explain all the decision making applied to the simulations in order to represent the closest results compared to scientific literature. After illustrating the experiment, governing equations of the chosen RANS and LES models, the picked OpenFoam solver are going to be presented. Later, transport properties together with discretization selection will be shown, followed by the mesh and boundary conditions.

4.1. Comparing Experiment

The experiments made by Shehata et al. [7], are used in this study as a comparison for model accuracy.
The experimental set-up is a very long pipe, with two distinctive section: first part is used for reaching fully developed flow, whereas the second one is heated to see the turbulent mixed convection in action. The geometry details are contained in the following table.

Table 4.1: Geometrical characteristics of experimental set-ups. Source: [7]

Geometrical Dimension	***[mm]***
Diameter (D)	27.4
Unheated length	1370 (=50 D)
Heated length	876.8 (=32D)

The fluid is air, inserted in the pipe at ambient temperature and pressure. Once the gas flows the entire tube length, it is exhausted again in the environment.
The paper classifies three different experiments with a number sequence, which identify the physical imposed conditions. These are now listed in Table 4.2.

Table 4.2: List of experimental set-ups. Source: [7]

Case	q^+	***Re***
445	0.0045	4000
618	0.0018	6000
635	0.0035	6000

q^+ is defined as:

$$q^+ = \frac{q_w}{GC_{p,in}T_{in}} \tag{4.1}$$

where G is the mean mass flux, T is temperature and in subscript indicates the inlet values.
Therefore form Table 4.1, three cases are going to be model: laminarizing (445), sub-turbulent (618) and turbulent (635) [7].
From Eq. 4.1 the maximum inlet velocity and the wall heat flux are calculated. Starting with G definition for a pipe geometry:

$$G = \frac{4\dot{m}}{\pi D^2} \quad with \quad \dot{m} = \iint \rho u \, dA \tag{4.2}$$

Hence, Reynolds number can be re-written:

$$Re = \frac{GD}{\mu} \tag{4.3}$$

Once G is calculated, despite Re is given and μ can be found by the CoolProp [10], which is a C++ code implementation on Excel that provides physical values dependent on environmental conditions, then the entering maximum velocity is:

$$U_{max} = \frac{G}{\rho} \tag{4.4}$$

Concerning the wall heat flux:

$$q_w = q^+ \cdot (GC_{p,in}T_{in}) \tag{4.5}$$

Same considerations of Eq. 4.4 are done for the one above: G is now known, $C_{p,in}$ is gained by the mean of CoolProp and T_{in} is the standard room temperature ($T = 298.15K$).
Consequently, the results for each case of this mathematical procedure are now given in Table.4.3.

Table 4.3: Resulting boundary conditions quantities from mathematical calculations

Case	$U_{max}(m/s)$	$q_w(W/m^2)$
445	2.7	3636.13
618	3.46	2181.68
635	3.46	4242.15

These quantities will be employed as boundary conditions for the simulations.

4.2. RANS chosen models

In this study three different RANS model are used to simulate the two-dimensional geometry. The next subsections will show the equations of these models and how they handle the closure problem.

4.2.1. Spalart and Allmaras Model

Starting with the one-equation model developed by Spalart and Allmaras [53], which from now on will be abbreviated with "SA". According to this model, the eddy viscosity is gained through the solution a new property, the modified turbulence viscosity $\tilde{\nu}$ as equated in Eq. 4.6.

$$\frac{\partial \tilde{\nu}}{\partial t} + u_j \frac{\partial \tilde{\nu}}{\partial x_j} = c_{b1}(1 - f_{t2})\tilde{S}\tilde{\nu} - \left[c_{w1}f_w - \frac{c_{b1}}{\kappa^2}f_{t2}\right]\left(\frac{\tilde{\nu}}{d}\right)^2 + \frac{1}{\sigma}\left[\frac{d}{\partial x_j}\left((\nu + \tilde{\nu})\frac{\partial \tilde{\nu}}{\partial x_j}\right] + c_{b2}\frac{\partial \tilde{\nu}}{\partial x_i}\frac{\partial \tilde{\nu}}{\partial x_i}\right. \tag{4.6}$$

Once Eq. 4.6 is solved, the turbulent viscosity is calculated by this system of equations:

$$\mu_t = \rho \tilde{\nu} f_{u1} \tag{4.7}$$

$$f_{u1} = \frac{\chi^3}{\chi^3 + c_{u1}^3} \tag{4.8}$$

$$\chi = \frac{\tilde{\nu}}{\nu} \tag{4.9}$$

The additional introduced terms corresponds to:

$$\tilde{S} = \Omega + \frac{\tilde{\nu}}{\kappa^2 d^2} f_{u2} \tag{4.10}$$

$$f_{u2} = 1 - \frac{\chi}{1 + \chi f_{u1}} \tag{4.11}$$

$$f_w = g\Big[\frac{1+c_{w3}^6}{g^6+c_{w3}^6}\Big]^{1/6} \tag{4.12}$$

$$g = r + c_{w2}(r^6 - r) \tag{4.13}$$

$$r = min\Big[\frac{\tilde{\nu}}{\tilde{S}\kappa^2 d^2}, 10\Big] \tag{4.14}$$

In the above equations, d is the distance from the field point to the nearest wall and $\Omega = \sqrt{2W_{ij}W_{ij}}$ is the vorticity magnitude, with W_{ij} defined as the following:

$$W_{ij} = \frac{1}{2}\Big(\frac{du_i}{dx_j} - \frac{du_j}{dx_i}\Big) \tag{4.15}$$

The rest are constants of the model, summarised in Table 4.4 below.

Table 4.4: List of SA constants. Source: [26]

Constant	***Value***
c_{w1}	$\frac{c_{b1}}{\kappa^2} + \frac{1+c_{b2}}{\sigma}$
c_{b1}	0.1355
c_{b2}	0.622
σ	2/3
κ	0.41
c_{w2}	0.3
c_{w3}	2
c_{u1}	7.1
c_{t3}	1.2
c_{t4}	0.5

4.2.2. k-ϵ Model

The $k-\epsilon$ is probably the most common two-equation turbulence model, invented by Launder and Spalding [17] also referred as *Standard* $k-\epsilon$. These model uses two additional equations for turbulent quantities: the turbulent kinetic energy (k) and the turbulent dissipation (ϵ). These variables are quantified by computing Eq. 4.14 and Eq. 4.15.

$$\frac{\partial(\rho k)}{\partial t} + \frac{\partial(\rho u_i k)}{\partial x_i} = \frac{\partial}{\partial x_j}\Big[\Big(\mu + \frac{\mu_t}{\sigma_k}\Big)\frac{\partial k}{\partial x_j}\Big] + P_k - \rho\epsilon \tag{4.16}$$

$$\frac{\partial(\rho\epsilon)}{\partial t} + \frac{\partial(\rho u_i \epsilon)}{\partial x_i} = \frac{\partial}{\partial x_j}\Big[\Big(\mu + \frac{\mu_t}{\sigma_k}\Big)\frac{\partial \epsilon}{\partial x_j}\Big] + \frac{c_{1\epsilon}}{k}\Big(P_k + \frac{2}{3}k\frac{\partial u_i}{\partial x_i}\Big) - c_{2\epsilon}\rho\frac{\epsilon^2}{k} \tag{4.17}$$

where P_k is the production term:

$$P_k = \rho\overline{u_i u_j}\frac{\partial \overline{u_i}}{\partial x_j} \tag{4.18}$$

From the equations written above, the eddy viscosity is gained by the next formulation:

$$\mu_t = \rho C_\mu \frac{k^2}{\epsilon} \tag{4.19}$$

Therefore, based on these definitions, Table.4.5 lists all the standard values of the model constants.

Table 4.5: List of $k-\epsilon$ constants. Source: [31]

Constant	***Value***
σ_k	1
σ_ϵ	1.3
$c_{1\epsilon}$	1.44
$c_{1\epsilon}$	1.92
c_μ	0.09

4.2.3. Menter Shear Stress Transport Model

The Menter Shear Stress Transport is another two-equation turbulence model, which is always referred to $k-\omega$ SST model. Invented by Menter [22], this model modifies the standard $k-\omega$, but still using the same turbulent quantities: the turbulent kinetic energy and the turbulent specific dissipation rate (ω). These variables are quantified by computing Eq. 4.18 and Eq. 4.19.

$$\frac{\partial(\rho k)}{\partial t}+\frac{\partial(\rho u_j k)}{\partial x_j}=P-\beta^*\rho\omega k+\frac{\partial}{\partial x_j}\Big[(\mu+\sigma_k\mu_t)\frac{\partial k}{\partial x_j}\Big] \tag{4.20}$$

$$\frac{\partial(\rho\omega)}{\partial t}+\frac{\partial(\rho u_j\omega)}{\partial x_j}=\frac{\gamma}{\nu_t}P-\beta_1\rho\omega^2+\frac{\partial}{\partial x_j}\Big[(\mu+\sigma_k\mu_t)\frac{\partial\omega}{\partial x_j}\Big]+2(1-F_1)\frac{\rho\omega_{\omega 2}}{\omega}\frac{\partial k}{\partial x_j}\frac{\partial\omega}{\partial x_j} \tag{4.21}$$

The term P is:

$$P=\tau_{ij}\frac{\partial u_i}{\partial x_j} \tag{4.22}$$

$$\tau_{ij}=\mu_t\Big(2S_{ij}-\frac{2}{3}\frac{\partial u_k}{\partial x_k}_{ij}\Big)-\frac{2}{3}\rho k\delta_{ij} \tag{4.23}$$

$$S_{ij}=\frac{1}{2}\Big(\frac{\partial u_i}{\partial x_j}+\frac{\partial u_j}{\partial x_i}\Big) \tag{4.24}$$

From the equations written above, the eddy viscosity is gained by the next formulation:

$$\mu_t=\frac{\rho\alpha_1 k}{max(\alpha_1\omega,\Omega F_2)} \tag{4.25}$$

Every constant with "1" as subscript is in function of another one denoted with "2", as showed for the generic ϕ in Eq. 2.24.

$$\phi=F_1\phi_1+(1-F_1)\phi_2 \tag{4.26}$$

with:

$$\begin{cases}F_1=tanh(arg_1^4) & \text{with} \quad arg_1=min\Big[max\Big(\frac{\sqrt{k}}{\beta^*\omega d},\frac{500\nu}{d^2\omega}\Big),\frac{4\rho\sigma_{\omega 2}k}{CD_{k\omega}d^2}\Big]\\ F_2=tanh(arg_2^2) & \text{with} \quad arg_2=max\Big(2\frac{\sqrt{k}}{\beta^*\omega d},\frac{500\nu}{d^2\omega}\Big)\end{cases} \tag{4.27}$$

Therefore, based on these definitions, Table.4.6 lists all the standard values of the model constants.

Table 4.6: List of $k-\omega SST$ constants. Source: [32]

Constant	***Value***
γ_1	$\frac{\beta_1}{\beta^*} - \frac{\sigma_{\omega 1}\kappa^2}{\sqrt{\beta^*}}$
γ_2	$\frac{\beta_2}{\beta^*} - \frac{\sigma_{\omega 2}\kappa^2}{\sqrt{\beta^*}}$
κ	0.41
σ_{k1}	0.85
σ_{k2}	1
$\sigma_{\omega 1}$	0.3
$\omega_{\omega 2}$	0.856
β_1	0.075
β_2	0.0828
β^*	0.09
α_1	0.31

4.3. LES chosen models

Concerning the LES simulations, the WALE model has been chosen, because it was demonstrated to be suitable for heated channel flows [50].
The WALE model evaluates the sub-grid scale eddy viscosity as [51]:

$$\nu_{sgs} = C_k \Delta \sqrt{k_{sgs}} \tag{4.28}$$

where C_k is a model constant, Δ is the grid size that defines the sub-grid length scale and k_{sgs} is the sub-grid scale kinetic energy, which is calculated like Eq. 27.

$$k_{sgs} = \Big(\frac{C_\omega^2 \Delta}{C_k}\Big)^2 \frac{(S_{ij}^d S_{ij}^d)^3}{\Big(([S_{ij}][S_{ij}])^{5/2} + (S_{ij}^d S_{ij}^d)^{5/4}\Big)^2} \tag{4.29}$$

with C_ω, $[S_{ij}]$ and S_{ij}^d corresponding respectively to another model constant, the filtered velocity stress tensor and the traceless symmetric part of the square of the velocity gradient tensor [70], equated as:

$$[S_{ij}] = \frac{1}{2}\Big(\frac{\partial [u_i]}{\partial x_j} + \frac{\partial [u_j]}{\partial x_i}\Big) \tag{4.30}$$

$$S_{ij}^d = \frac{1}{2}\Big(\frac{\partial [u_k]}{\partial x_i}\frac{\partial [u_j]}{\partial x_k} + \frac{\partial [u_k]}{\partial x_j}\frac{\partial [u_i]}{\partial x_k}\Big) - \frac{1}{3}\delta_{ij}\frac{\partial [u_k]}{\partial x_k}\frac{\partial [u_k]}{\partial x_k} \tag{4.31}$$

About the model constants, they all lists in the following Table 4.7.

Table 4.7: List of WALE constants. Source: [27]

Constant	***Value***
C_k	0.094
C_ω	0.325

4.4. Solver

The study has been performed using OpenFOAM, a free and open source CFD software that allows the user to modify or create new solvers. In OpenFOAM solvers are categorised on the analysis that has to be done on the simulation [30]. Therefore, for this research the most suitable solvers are presented in “Heat transfer and buoyancy-driven flows” category. Specifically, the "buoyantBoussinesqPimpleFoam" was selected and further modified for the study. The solver simulates a transient and turbulent system, where an incompressible fluids interacts with buoyancy [29]. Hence, the mass and momentum conservation are [71]:

$$\frac{\partial \rho}{\partial t} + \nabla \cdot (\rho u) = 0 \tag{4.32}$$

$$\frac{\partial(\rho u)}{\partial t} + \nabla \cdot (\rho u u) = -\nabla p + \rho g + \nabla \cdot \left(2\mu_{eff} D(u)\right) \tag{4.33}$$

μ_{eff} the sum of molecular (μ) and turbulent viscosity (μ_t), also called the effective viscosity. Therefore, its definition is:

$$\nu_{eff} = \nu + \nu_t \tag{4.34}$$

The other important term is $D(u)$, which is the rate of strain tensor, described by Eq. 4.33.

$$D(u) = \frac{1}{2}(\nabla u + (\nabla u)^T) \tag{4.35}$$

However recalling Eq. 2.9, once the Boussinesq approximation is applied and the pressure term is arranged as P_{rgh} according to OpenFoam way of calculation, the equations look like:

$$\nabla \cdot u = 0 \tag{4.36}$$

$$\frac{\partial u}{\partial t} + \nabla \cdot (uu) = -\nabla p_{rgh} - (g \cdot r)\nabla\left(\frac{\rho}{\rho_0}\right) + \nabla \cdot \left(2\nu_{eff} D(u)\right) \tag{4.37}$$

ν_{eff} the sum of molecular (ν) and turbulent viscosity (ν_t). Hence looking at the equations, density has been simplified everywhere because it is considered a constant, except for $p_{rgh} = (p - \rho g \cdot r/\rho_0)$ and $\nabla(\rho/\rho_0)$, where its temperature dependence is evaluated. Furthermore, r has been introduced as position vector. Applying the same simplifications to the temperature equations, it will look like:

$$\frac{\partial \theta}{\partial t} + \nabla \cdot (u\theta) = \alpha_{eff} \nabla^2 \theta \tag{4.38}$$

Again, the subscript eff states for effective. Indeed, Eq. 4.37 defines the thermal effective diffusivity (α_{eff}) as the effective viscosity in Eq. 4.32.

$$\alpha_{eff} = \alpha + \alpha_t \tag{4.39}$$

However, the solver calculates the two components using the definition of Prandtl number:

$$Pr = \frac{\nu}{\alpha} \quad \rightarrow \quad \alpha = Pr/\nu \tag{4.40}$$

$$Pr_t = \frac{\nu_t}{\alpha_t} \quad \rightarrow \quad \alpha_t = Pr_t/\nu_t \tag{4.41}$$

It is very common to consider Eq. 4.39 constant for reducing computational effort, even though it is not.

$$Pr_t = \frac{\overline{u_i' u_j'}}{\overline{u_j' T'}} \frac{d\overline{T}/dx_j}{d\overline{u_j}/dx_j} \tag{4.42}$$

Indeed, the Pr_t represent the ratio between turbulent stresses and heat flux (Eq. 4.40), which in reality varies over space and time. Same process is applied to LES, just substituting ν_t and α_t with ν_{SGS} and α_{SGS}.

4.5. Transport properties

The transport properties dictionary requires the physical properties that characterizes the fluid. As previously introduced, for calculation simplicity the molecular and turbulent Prandtl number are set constant with the following values:

$$Pr = 0.75 \tag{4.43}$$

$$Pr_t = 0.85 \tag{4.44}$$

Concerning the former, the choice is properly made due to the fact that its variations are quite small compared to temperature increment, as shown in Fig. 4.1 below.

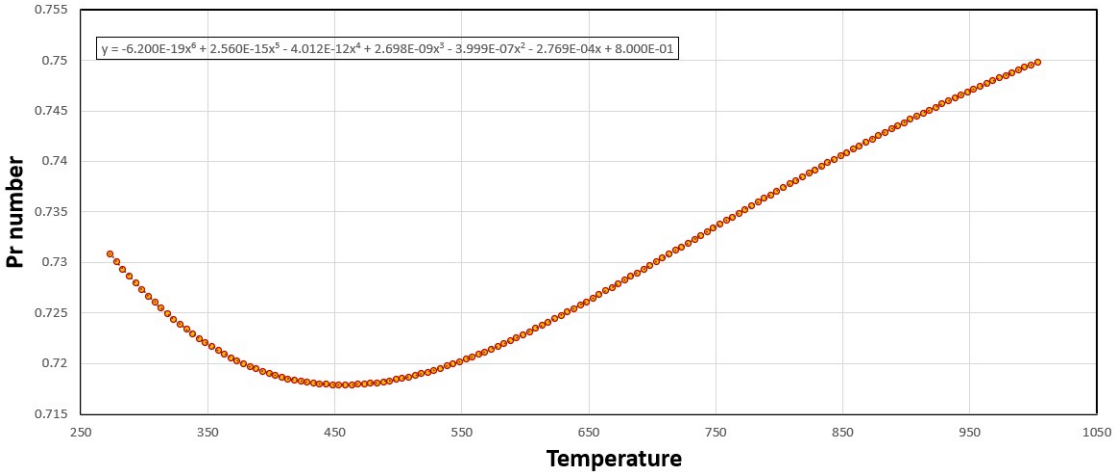

Figure 4.1: Prandtl number versus temperature, plotted through CoolProp

About the latter, in forced convection Pr_t is assumed as a specific value for each different turbulent flow (i.e. 0.5 for a planar jet [8]), but it cannot be less than 0.05 according to experiment data collected by [76]. In this specific case, thermal and inertial stresses varies remarkably, making it technically not constant. However, according to the scientific literature [49], 0.85 should give the accurate results in the most variety cases, especially close to the walls [38] [67], avoiding a higher computational effort.
Another requirement is the law for viscosity, which is usually Newtonian. This function assumes a constant dynamic viscosity over time and space. Nevertheless, in order to gain more preciseness during the calculations, a new transport model is implemented. This is base on a polynomial function dependent on temperature built by the way of CoolProp and plotted in Fig. 4.2.
Therefore, once the solver find the temperature, it is inserted in the equation and the new viscosity is available for next iteration. The entire code can be found in the Appendix.
A third function is coded, this time creating a new field in the solver algorithm. This describes the thermal conductivity of air, again based on temperature and also found with CoolProp. It can be visualised in Fig. 4.3.

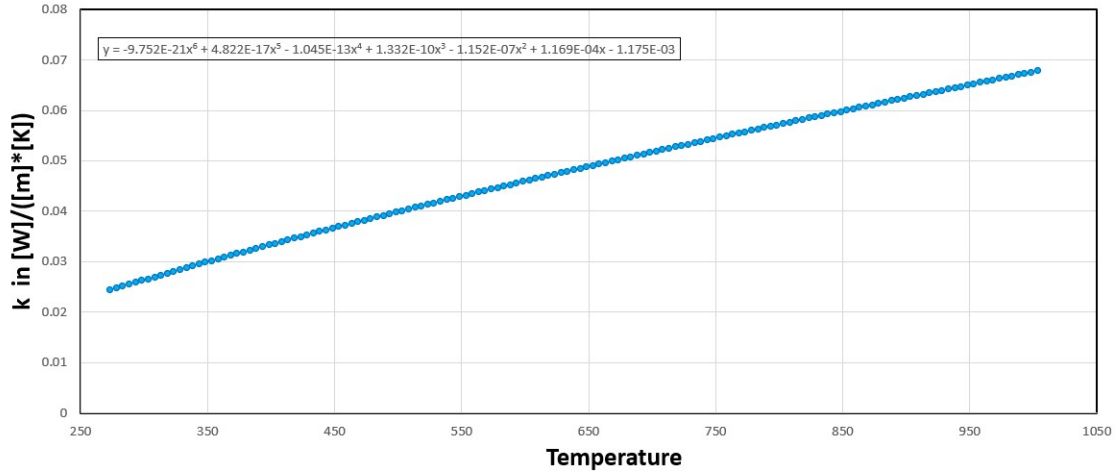

Figure 4.2: Thermal diffusivity versus temperature, plotted through CoolProp

The variable k is not involved in the temperature conservation, it is only used for the wall boundary condition in order to impose a fixed heat flux. Further considerations are presented into the Boundary Conditions section.

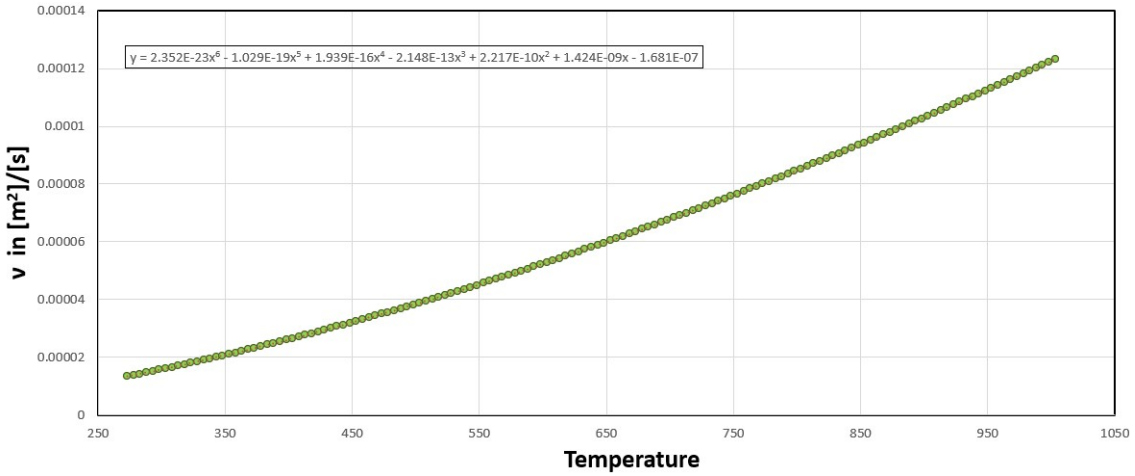

Figure 4.3: Dynamic viscosity versus temperature, plotted through CoolProp

4.6. Numerical Scheme

Another directory included in "system" folder, is the “fvSchemes” dictionary, which instruct the solver which numerical schemes to use for every physical quantity that belongs to Navier-Stokes equations.

4.6.1. Time Schemes

Selected inside “ddtSchemes”, it solves time derivatives (d/dt) in the equations. The "backward" time scheme was chosen for all simulations, which is a second order, transient and implicit scheme. Even if boundedness not guaranteed, this scheme was employed for stability reasons [34].

4.6.2. Gradient Schemes

The used discretization technique for gradients (∇) is the standard finite volume Gaussian integration. This scheme requires interpolation of cell centres to face centres quantities; this is why an interpolation scheme is required as well. In all the simulations performed a linear interpolation scheme was chosen ("Gauss linear").

4.6.3. Divergence Schemes

As in the previous sub-dictionary the Gauss scheme was picked for the discretization of divergence ($\nabla\cdot$) terms. Again, an interpolation scheme also must be chosen and for every physical property of the equations. The default one was set "Gauss upwind", where “Upwind” is a first-order bounded divergence scheme in which the up-stream variables are used to calculate the derivatives in the flow field. Gauss Linear was applied only for $div(phi \cdot u)$ with $phi = \rho U$ (mass flux) and the strain tensor, in order to gain stability during the calculation.

4.6.4. Laplacian Schemes

Concerning the laplacian operations (∇^2), "Gauss linear corrected" is set to standard choice. The keyword “corrected” states for an explicit non-orthogonal correction, that activates when the vector connecting cell centres is non-orthogonal, meaning it deviates from the orthogonal scheme.

4.6.5. Surface Normal Gradient Schemes

The component of each gradient that is normal to a cell face is solved under schemes specified in this sub-dictionary. Required as an additional entry in the Laplacian Schemes shown above, the scheme of selection in our simulations was the “corrected” scheme, which refers to an explicit non-orthogonal correction.

4.7. Solution

The equation solvers and tolerances are in another folder called “fvSolution”, which also belongs to the “system” directory. The term “solvers” in this case specified the “linear solvers” that are used to discretize the entire equation itself. Now, the next two sub-sections will explained the specific selection for this research.

4.7.1. Solvers

In the main sub-dictionary space, the linear solver are required for each discretised equation that must be solved. An Example is given by Fig. 4.4 and Fig. 4.5.

```
"(p|p_rgh)"
{
  solver          GAMG;
  tolerance       1e-6;
  relTol          0.01;
  smoother        DICGaussSeidel;
  minIter         1;
  maxIter         100;
  nPreSweeps      1;
  nPostSweeps     3;
  nFinestSweeps   3;
  scaleCorrection true;
  directSolveCoarsest     false;
  cacheAgglomeration      on;
  nCellsInCoarsestLevel   50;
  agglomerator    faceAreaPair;
  mergeLevels     1;
}
```

Figure 4.4: Linear solver for symmetric matrices like pressures

Looking at the figures, the first line indicates the selection of the linear solver for symmetric matrices like Geometric agglomerated Algebraic Multi-Grid (GAMG), or for asymmetric matrices like the Stabilized Preconditioned (bi-) conjugate gradient (PBiCGStab).
Then, the second entry is where the pre-conditioner is specified. Again, there are two choices which are based on matrix shape of the physical fields: the Diagonal incomplete-Cholesky (DIC) in case of symmetry or the Diagonal incomplete-LU (DILU) for asymmetric ones.

```
"(U|h|e|k|omega|R|T)"
{
    solver          PBiCGStab;
    preconditioner  DILU;
    tolerance       1e-6;
    relTol          0.1;
}
```

Figure 4.5: Linear solver for symmetric matrices

At the end of every iteration, the error is calculated by residuals evaluation and compare them to the tolerance specified by the user. Obviously, accuracy is proportional to smaller set tolerance quantities. Specifically, from Fig. 4.4 and Fig. 4.5 can be seen that two tolerances must be calibrated: “tolerance” and “relTol”. The solver stops calculating either when the last iteration residual values are below specified “tolerance” or when the ratio between current and initial residuals drops under the set relative tolerance “relTol”.

4.7.2. Relaxation – Algorithm Control

Two additional options are inside "fvSolution":

1. ***Under-Relaxation Control***: a technique which aims computational stability by specifying “relaxation factors” for each equation or field [33].

2. ***Algorithm Control***: The algorithm is the one in charge of solving the velocity-pressure field correlation [28]. Furthermore, three types of correctors can be specified:

    - *nOuterCorrectors*: It quantifies the number of iterations to process each time step.
    - *nCorrectors*: They are also called inner correctors and they defines number of pressure corrections for a single iteration.

- *nNonOrthogonalCorrectors*: It corrects in case of mesh non-orthogonality.

In the current study, none of relaxation factors are used. Concerning the pressure-velocity coupling, the PIMPLE algorithm is used, which combines the "PISO" (Pressure Implicit with Splitting of Operator) and the "SIMPLE" (Semi-Implicit Method for Pressure-Linked Equations) methods [25].

4.8. Mesh

The introduced rapid gradient of temperature and velocity at the wall need to be handled in CFD with a finer mesh, which depends on y^+ [66]:

$$y^+ = \Delta y \frac{u_\tau}{\nu} \tag{4.45}$$

where Δy is the distance from the first cell to the nearest wall and u_τ is the shear velocity, equated below.

$$u_\tau = \sqrt{\frac{\tau}{\rho}} \tag{4.46}$$

The term y^+ determines the different length scales governing the velocity profile equations [23], which is shown in Fig. 4.6.

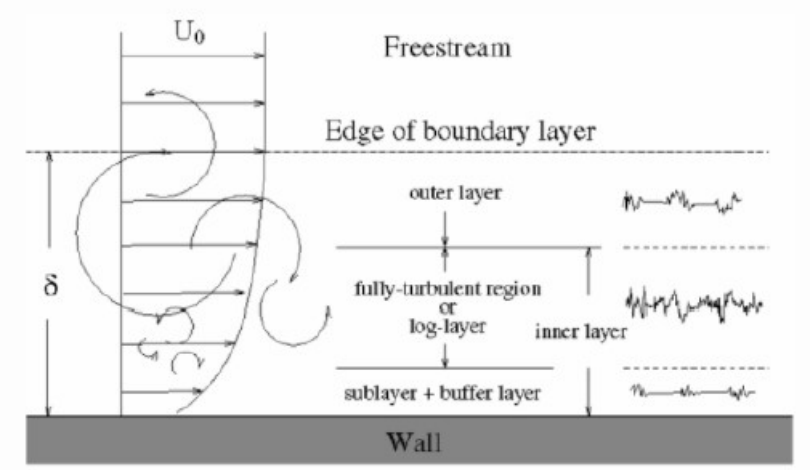

Figure 4.6: Variety of velocity scales when a turbulent boundary layer occurs [46]

Precisely, the important length scale is the buffer layer, because it is where turbulence is generated and the region in which turbulent and viscous stresses are equally important [23], as plotted by region IV in Fig. 4.7.

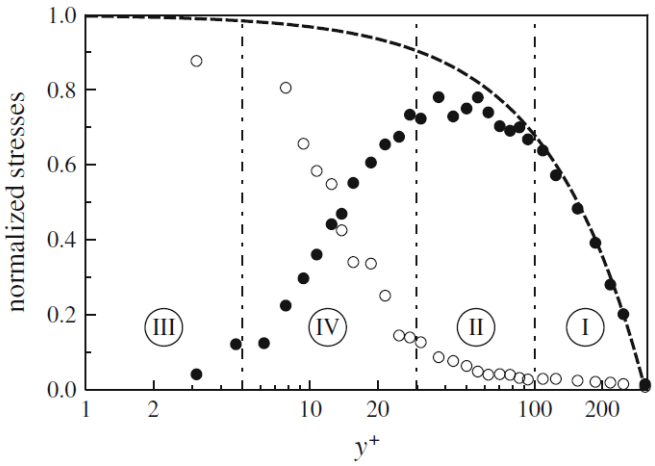

Figure 4.7: Shear stress versus the dimensionless distance y^+ in a semi-log plot at $Re = 10,000$. At $r = 0$ corresponds to $y^+ = 312$ and $r = D/2$ to $y^+ = 0$. I=core region, II=logarithmic wall region, III=viscous sub-layer and IV=buffer layer. Black dotes=Reynolds stresses/u_*^2 and white dotes=Viscous stresses/u_*^2. Source: [23]

The viscous sub-layer (region III in Fig. 4.7) is the Kolmogorov scale, a quite difficult phenomenon to handle for CFD software. This is the reason why "wall functions" are usually set as boundary conditions at the wall, which solves the flow on the base of empirical conditions. However, to reach an acceptable accuracy, it is suggested to reach $\Delta y^+ \leq 1$, especially for LES simulations [66].
In order to satisfy this requirement the Moody chart has been used (Fig. 4.8). From the diagram, the skin friction factor or Fanning factor (f) can be feasibly found or the following equation can be used in case of turbulent pipe flow [57]:

$$\frac{1}{\sqrt{f}} = -2log\Big(\frac{2.51}{Re\sqrt{f}}\Big) \tag{4.47}$$

Now that the values is known, it is then inserted in Eq. 4.46 to calculate the shear stress.

$$\tau = \frac{1}{2} f \rho U_0^2 \tag{4.48}$$

where U_0 is the maximum inlet velocity.

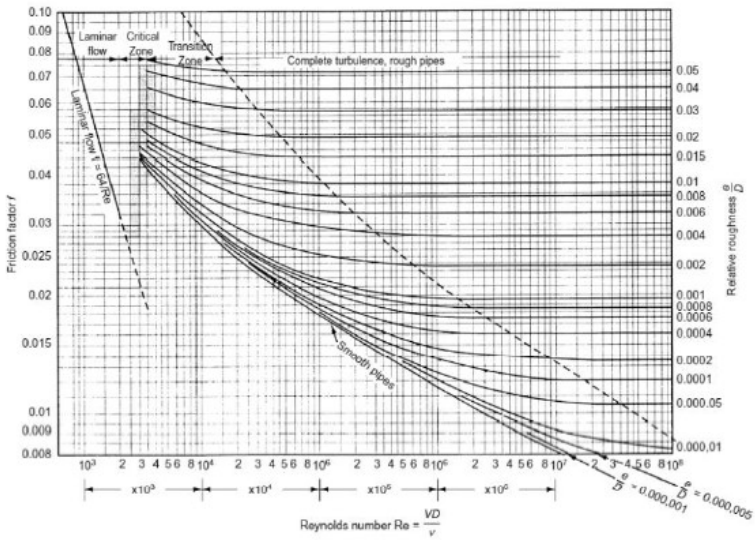

Figure 4.8: Moody diagram: it correlates the Darcy–Weisbach friction factor (f) with Reynolds number (Re) and surface roughness (ϵ) for fully developed flow in a circular pipe. Source: [16]

From it, recalling the Eq. 4.43, the maximum distance form the wall that characterizes the first cell can be calculated.
In conclusion, it must be specified that mesh refinement affects the solution until a certain limit, over which the improvement of the calculation accuracy is infinitesimal and definitely not convenient in regards to computational effort, according to Richardson extrapolation [1]. If this limit is achieved and/or exceed the solution is defined as mesh independent and this should be the project goal.

4.8.1. RANS Mesh

In details, for RANS simulation the approach is based on exploiting the small computational effort required by the solver. Therefore, since the problem and associated physical averaged quantities are axis-symmetric, the pipe was simplified by two-dimensional wedge geometry that represents only a slice of the total cylinder. The different geometry perspectives can be visualised in Fig. 4.9, Fig. 4.10 and Fig. 4.11.

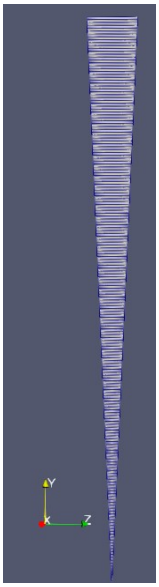

Figure 4.9: Front view of the wedge geometry

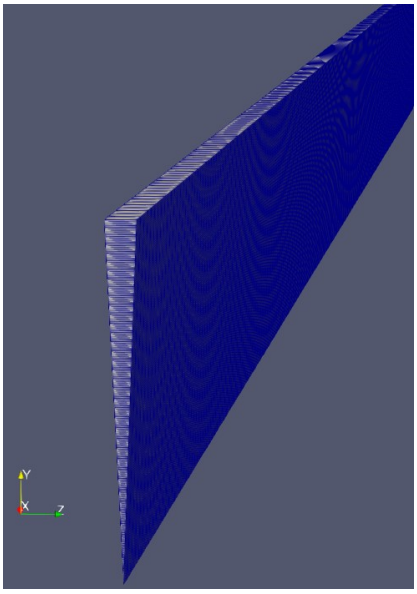

Figure 4.10: View of the wedge geometry that captures the one cell thickness in z-direction

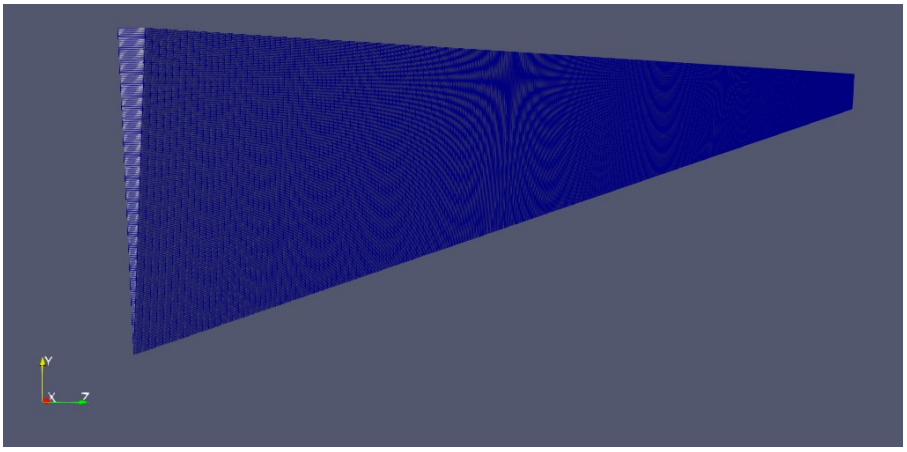

Figure 4.11: Side view of the wedge geometry

From Fig. 4.10, it is notable a one cell thickness along the z-direction, which is the way OpenFoam handles the 2D simulations. The flow is in the x-direction, where two symmetric inclined walls represents the wedge, a cyclical boundary condition that OpenFoam employs for solving twodimensional cylindrical problems.

In y direction, the number of cells depends on the dimensionless wall distance y^+, in order to properly catch the viscous sub-layer, as explained before. The following Table 4.8 gives to the reader the resulting mesh.

Table 4.8: List of wedge mesh specifications

Variable	***Value***
Number of Cells in x-direction	600
Number of Cells in y-direction	200
Number of Cells in z-direction	1

4.8.2. LES Mesh

Concerning the 3D geometry, the structure of the mesh is not constructed with a basic circle, in order to avoid a very small mesh size at the core as showed Fig. 4.12, resulting in too rough estimation of the solution.

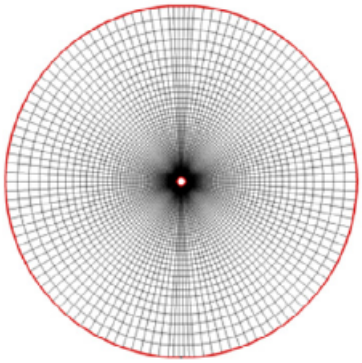

Figure 4.12: Example to avoid for building a regular mesh

In contrast, firstly a square circumscribed into the cross section of the simulated pipe was built, than 4 sectors that surrounds the square and compose the external diameter of the experimental tube (Fig. 4.13).

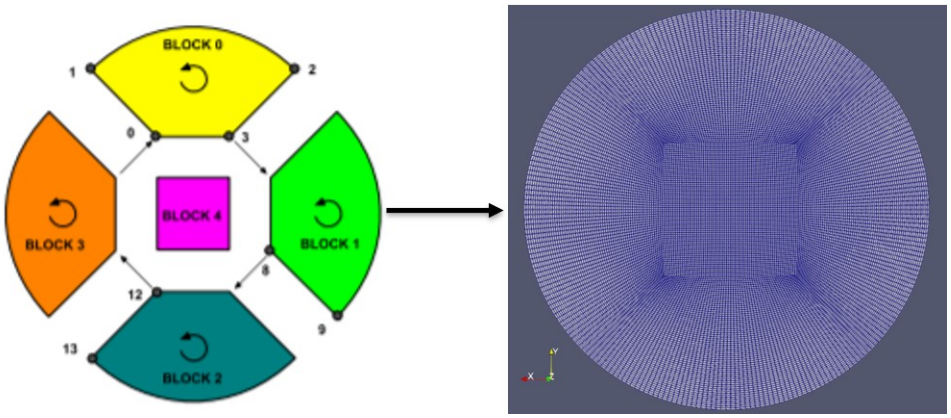

Figure 4.13: From left to right: method used to build the mesh and the final result

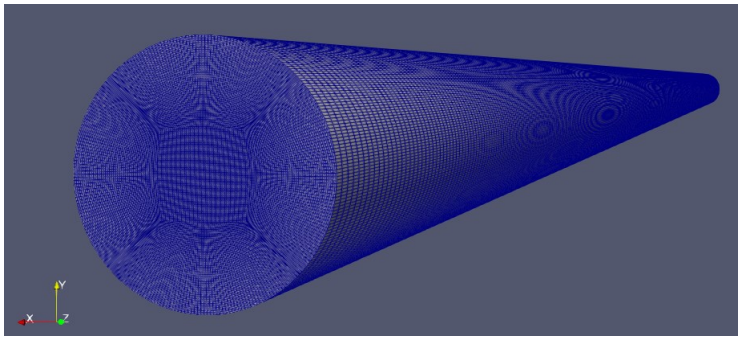

Figure 4.14: Side view of the 3D cylinder mesh

Again the y^+ was estimated as in the RANS simulations, resulting in the next table parameters.

Table 4.9: List of 3D mesh specifications

Variable	***Number of cells in x-direction***	***Number of cells in y-direction***	***Number of cells in z-direction***
Square	64	64	600
Per Sector	64	64	600

4.9. Boundary Conditions

The boundary conditions were approximately the same for both 2D and 3D simulations, except for the velocity inlet which needs a special treatment for LES models.
Beginning with p, p_{rgh}, ν_t, α_t and T, which have same impositions for every case:

Table 4.10: List of common boundary conditions

Variable	***Inlet***	***Wall***	***Outlet***
p	fixedGradient	zeroGradient	fixedValue (=0)
p_{rgh}	fixedFluxPresseure	fixedFluxPressure	fixedValue (=0)
T	fixedValue (298.15)	codedMixed	zeroGradient
ν_t	calculated	nutkWallFunction	calculated
α_t	calculated	alphatJaytillekeWallFunction	calculated

The "codedMixed" type describes a small piece of code that ensures the Fourier law application [48]:

$$q = -k\frac{dT}{dn} \tag{4.49}$$

where q is the heat flux and dT/dn is the normal component of the temperature gradient.
Recalling transport properties section, k was specified as temperature dependent polynomial function. The heat flux is imposed as a constant, thus the temperature gradient and k will change in order to respect Eq. 4.47 equality. In the Appendix can be found the written code, which also explains how OpenFOAM handle these kind of calculations.
Concerning $k-\omega SST$ model, also the turbulent kinetic energy and its dissipation rate need boundary conditions, listed in Table.4.11.

Table 4.11: List of added boundary conditions for $k-\omega SST$

Variable	***Inlet***	***Wall***	***Outlet***
k	fixedValue (=0.045 or 0.02 for 445 case)	kqRWallFunction	zeroGradient
ω	fixedValue (=14.35 or 9.42 for 445 case)	omegaWallFunction	zeroGradient

The "fixed values" at the inlet are calculated as suggested by OpenFOAM user guide [31].

$$k = \frac{3}{2}(I|u_{max}|)^2 \tag{4.50}$$

$$\omega = \frac{k^{0.5}}{C_\mu^{0.25} D} \tag{4.51}$$

where I is the intensity. Concerning $k-\epsilon$, the boundary conditions are exactly the same of $k-\omega SST$ model with ϵ instead of ω, like Table 4.12 shows.

Table 4.12: List of added boundary conditions for $k-\epsilon$

Variable	***Inlet***	***Wall***	***Outlet***
k	fixedValue (=0.045 or 0.02 for 445 case)	kqRWallFunction	zeroGradient
epsilon	fixedValue (=0.57 or 0.17 for 445 case)	epsilonWallFunction	zeroGradient

The inlet value for epsilon has been evluated with Eq. 4.50.

$$\epsilon = \frac{C_\mu^{0.75} k^{1.5}}{D} \tag{4.52}$$

Lastly, SA requires restriction for the added equation of $\tilde{\nu}$, illustrated by Table 4.13.

Table 4.13: List of added boundary conditions for SA

Variable	***Inlet***	***Wall***	***Outlet***
$\tilde{\nu}$	FixedValue (=3e-5)	zeroGradient	fixedValue (=0)

As stated at the beginning of this chapter, velocity makes the difference between RANS and LES boundary conditions, which will be explained in details in following sections.
However, wall and outlet are still the same, schematically summarised by Table 4.14.

Table 4.14: List of velocity boundary conditions for RANS and LES simulations

Variable	***Inlet***	***Wall***	***Outlet***
U_{RANS}	codedFixedValue	noSlip	zeroGradient
U_{LES}	timeVaryingMappedFixedValue	noSlip	zeroGradient

4.9.1. RANS velocity Inlet

The simulation should be a pipe with length of more than two meters in order to perfectly match with the experimental set-up. However, this would require an unnecessary amount of mesh cells, thus a computational effort that would rise the calculation time dramatically.
Instead, the geometry was shortened by a quantity slightly higher than the heated length (32 D = 876.8). Indeed, the pipe is 900 mm long, in order to let the flow developed properly towards the outlet and away the last axial location at which results are compared (x/D = 24.5). This choice has been made to not influence the results, which might be affected by the flow pattern influenced by "zeroGradient" boundary condition or in the worst scenario by reverse flow.
Hence, the inlet condition is a fully developed velocity profile, which in case of a pipe is shaped as a parabola [55], as shown by Eq. 4.51.

$$u = u_{max}\left[1 - \left(\frac{r}{R}\right)^2\right] \tag{4.53}$$

Furthermore, the non-heated pipe length is used by Shehata et al. [3] to allow flow development, which will be already turbulent. Thus, according to Fig. 4.15, the parabola will be flatten at the center flow.

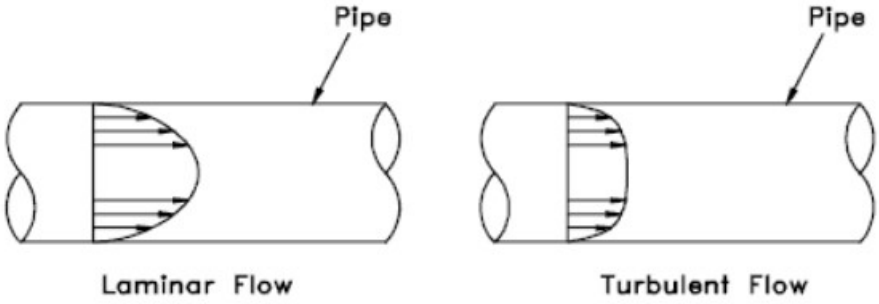

Figure 4.15: Difference of averaged velocity profile between laminar and turbulent flow inside a pipe [52]

Mathematically, it is traduces into a power law formula [60]:

$$u = u_{max}\left[1 - \left(\frac{r}{R}\right)^2\right]^n \tag{4.54}$$

The power coefficient is calculated by the following equations:

$$n = 1.03 \cdot ln(Re) - 3.6 \tag{4.55}$$

As a result the power coefficient is evaluated as constant n = 5.5 and n = 5 for 445 case. The "coded-FixedValue" gives to the user the opportunity to equate the parabola as the inlet, which is illustrated in the Appendix.

4.9.2. LES velocity Inlet

The LES case, requires a particular data set for the velocity inlet. This method is a simplification of the implementation proposed by Lund et al. [64], a scaled mapping of the velocity field from some plane of another simulation. Particularly, another cyclic pipe was iterated without heating walls and with the same solver. Furthermore, same radius of the final LES simulation, that is then compared with experimental data, was used but different length. Dimensions of the geometrical domain are summarised in Table 4.15.

Table 4.15: Geometrical characteristics of the cyclic pipe

Geometrical Dimension	***[mm]***
Diameter (D)	27.4
Unheated length	200 (=7.3 D)

The length is the minimum to ensure that outlet does not affect in any way the inlet flow.
Furthermore, the cyclic pipe present the same mesh radial distribution and iteration time step in order to remove the need for temporal or spatial interpolation during the mapping translation. The mesh specifications are listed in Table 4.16.

Table 4.16: List of 3D mesh specifications

Variable	***Number of cells in x-direction***	***Number of cells in y-direction***	***Number of cells in z-direction***
Square	64	64	250
Per Sector	64	64	250

The boundary conditions are described in Table 4.17.

Table 4.17: List of common boundary conditions

Variable	***Inlet***	***Wall***	***Outlet***
U	cyclic	noSlip	cyclic
p	cyclic	zeroGradient	cyclic
p_{rgh}	cyclic	fixedFluxPressure	cyclic
T	cyclic	codedMixed	cyclic
ν_t	cyclic	nutkWallFunction	cyclic
α_t	cyclic	alphatJaytillekeWallFunction	cyclic

Specifically for this cyclic case, a pressure drop or source term forcing a given mass flow must be prescribed as the driving force, otherwise the flow slows down to zero. This is made adding a new dictionary called "fvOptions" under the system folder, calculating it by the Hagen–Poiseuille equation [55].

$$\frac{\partial p}{\partial z} = \frac{8\mu \cdot u}{R^2} \tag{4.56}$$

The data is gain from a plane placed exactly in the middle of the cyclic pipe. Only velocity was stored, despite the fact that pressure has "zeroGradient" boundary condition at the inlet, which implies an absence of super-imposing a specific value. The process is visualised in Fig. 4.16.

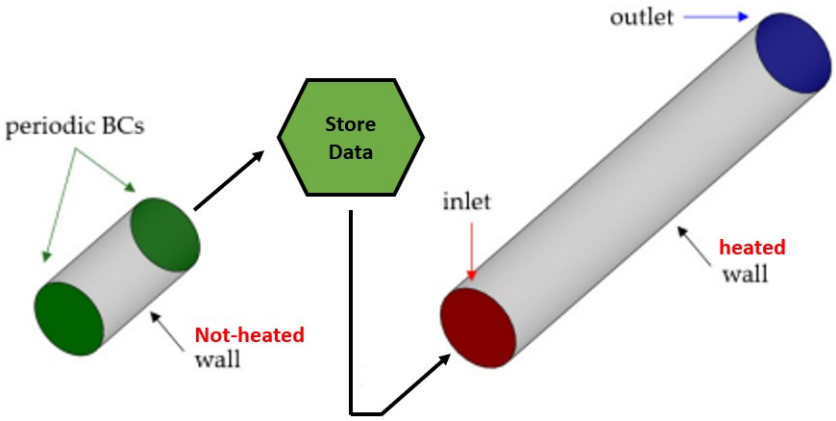

Figure 4.16: Velocity implementation for LES simulation, using cyclic simulation to generate the data set [35]

Map Scaling is used to enforce a specified bulk flow rate [15] and to approximate a growing boundary layer, which surely occur in a pipe. Finally, the computational cost and storage space are usually modest, which make this procedure really valuable for a better accuracy.

5

Results

The current chapter describes the outcome of the performed simulations, dividing results analysis in main four sections: the comparison between the two- and the three-dimensional geometry, the results of RANS simulations, the differences of the LES set-up from the real data and finally the role of gravity inside pipe flow.

5.1. RANS and LES Results Differences

In Chapter 3, it was introduced the approximation of the solution for RANS and LES models. The total simplification of the RANS equations for any vortex scale is clearly reflected in Fig. 5.1.

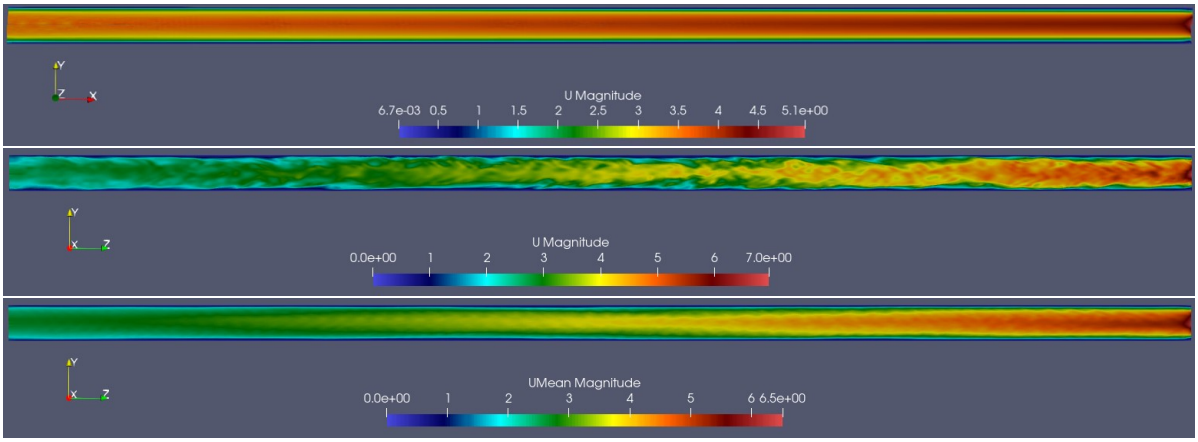

Figure 5.1: Velocity contours of the 635 case. From top to bottom: Wedge with RANS SST $k-\omega$ model, 3D with LES WALE and 3D with LES WALE and arithmetic mean results

The thermal acceleration of the flow is visible in both cases. However, the 2D simulation do not show any sign of vortex structures, in contrast with the LES. This happens because RANS models all eddy diffusivities, whereas LES solves directly large scale vortexes and approximates small ones. Furthermore, comparing average LES velocity field with the RANS one, it can be concluded that qualitatively are similar but quantitatively are very different, with a clear underestimation made by RANS.
Looking at the temperature contours in Fig. 5.2, same considerations given for velocity field can also be applied here. Again the RANS case displays a smooth boundary layer, in contrast with the wavy one predicted by LES set-up. Furthermore, the thermal boundary layer thickness (δ_T) is equal to the pipe diameter, which will dramatically rise temperature values at the core flow.
The temperatures provided by the LES simulation are lower than RANS, which might be caused by an overestimation of thermal diffusivity due to an extremely fast thermal boundary layer development.

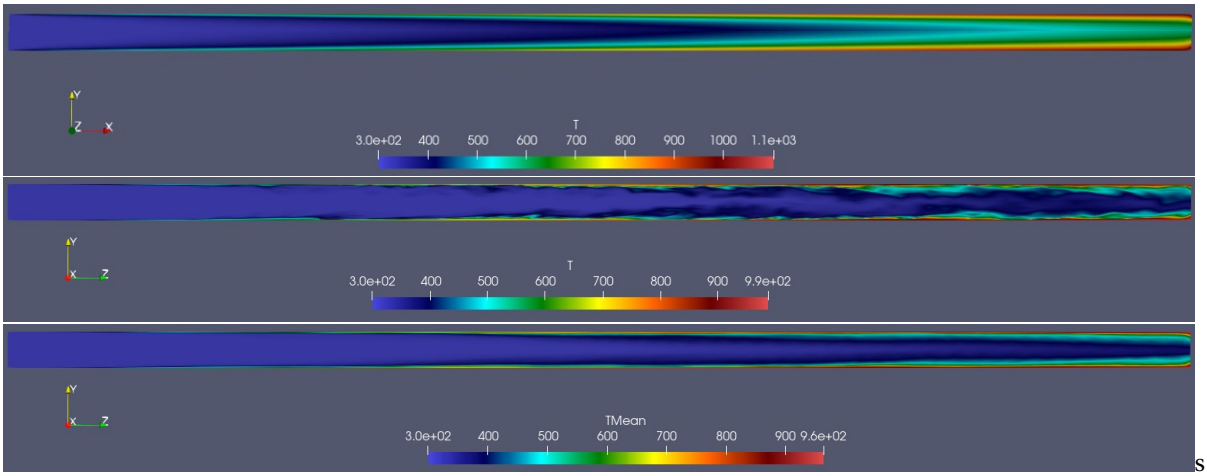

Figure 5.2: Temperature contours of the 635 case. From top to bottom: Wedge with RANS SST $k-\omega$ model, 3D with LES WALE and 3D with LES WALE and arithmetic mean results

In the following sections, results accuracy given by the 2D and 3D simulations will be measured through the radial distribution (y/R) of the ratio between the local temperature and the inlet one (T/T_{in}), comparing them to the experimental results [3].

5.2. RANS Results

As previously mentioned, the two-dimensional simulations are performed with three different RANS models: SST k-ω, Spalart-Allmaras and k-ϵ. Starting with the 618 case, Fig. 5.3 illustrates that close to the inlet ($x/D = 3.2$) the thermal boundary layer is very thin, since the heat flux is low.

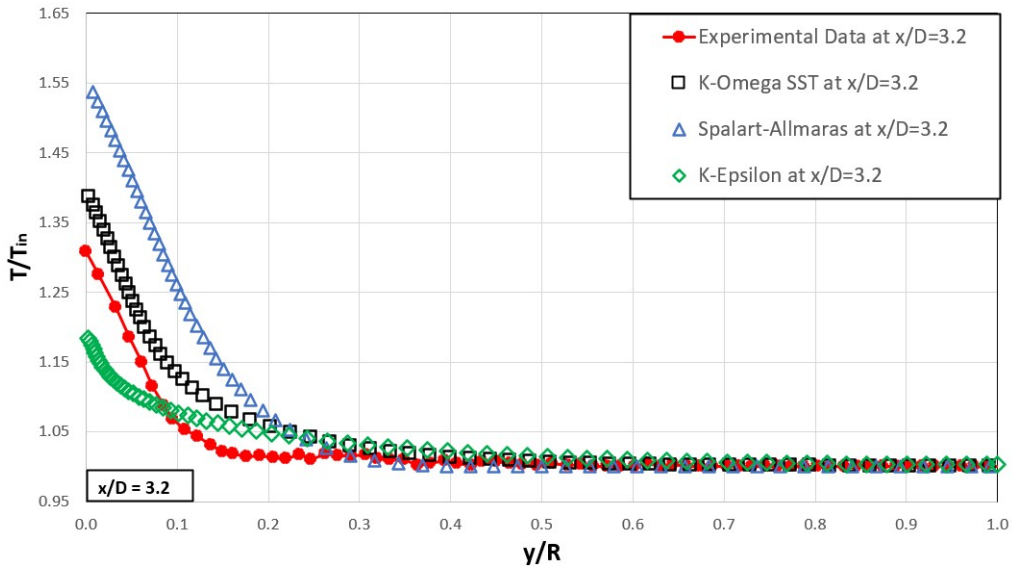

Figure 5.3: Comparison of RANS models and experimental data of normalised temperature field for 618 case at x/D = 3.2

The k-ω SST and the Spalart-Allmaras are able to approximate the curve trend, reaching the maximum overestimation at $y/R = 0$ of 8% and a considerable 19%, respectively. At the same time, k-ϵ is even more unreliable for both qualitative and quantitative results, due to the the notorious incapability of properly solving Navier-Stokes equations at the walls [14], making its use inappropriate for internal flows.
At almost half of the pipe length ($x/D = 14.2$) the only acceptable results are coming from k-ω SST. In Fig. 5.4 is visible that Spalart-Allmaras gives higher values not only at the wall but also at the center of the flow.

This happens because the model wrongly translate buoyancy effects into a rise of viscosity. Therefore, the incorrect α estimation results in excessive temperature values even towards the pipe axis [43].
Indeed, RANS models struggle to deliver appropriate density distributions [66], underestimating them in the wall region, worsen by the employment of Boussinesq approximation. As a consequence, the turbulence flow structure is strongly affected because the thermal acceleration is undervalued (visualised by Fig. 5.1) [73], whereas the temperature is widely enhanced by the wrong calculated thermal diffusivity.

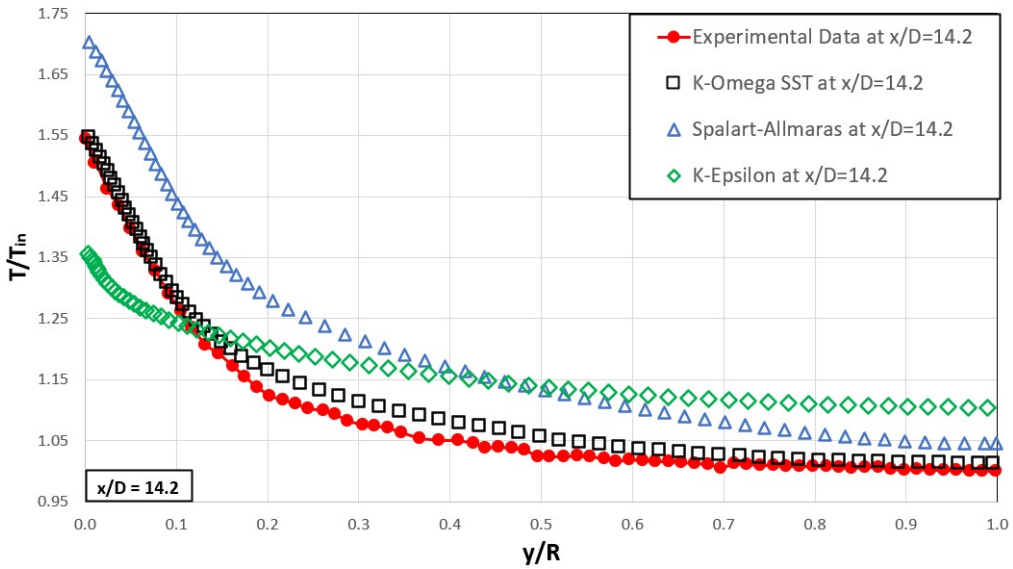

Figure 5.4: Comparison of RANS models and experimental data of normalised temperature field for 618 case at x/D = 14.2

The effects of this error are even more clear at the end of the pipe ($x/D = 24.5$) as shown by Fig. 5.5, where forces are even stronger than upstream due to the thicker boundary layers.

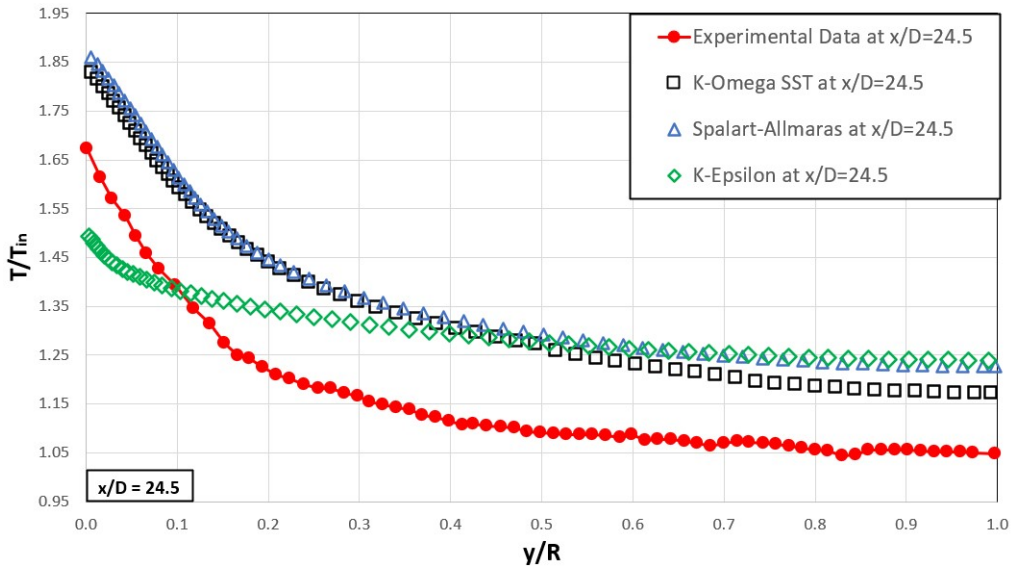

Figure 5.5: Comparison of RANS models and experimental data of normalised temperature field for 618 case at x/D = 24.5

Indeed according to the Eq. 5.1, boundary layer thickness is directly correlated to a substantial rise of viscosity [48].

$$\delta_v(x) \approx const. \cdot \sqrt[1/5]{\frac{\nu x}{U}} \tag{5.1}$$

Indirectly, α also grows according to Eq. 5.2, despite Pr is kept constant, leading again to an overestimation of the temperature filed, ignoring gravity effects.

$$\frac{\delta_v}{\delta_T} \approx Pr^{1/3} \tag{5.2}$$

The pattern at the three different axial locations exhibited by the 618 case is emphasised when the heat flux is increased, such as the 445 case. The reduction of the Reynolds number, therefore the maximum velocity, and almost doubling the heat flux compared the previous simulation provides unacceptable physical behaviour since the beginning (Fig. 5.6). The reason is again the thicker thermal boundary layer that develops at the inlet because of the larger gradients of temperature between the center flow and the heated walls. In fact looking again at Eq. 5.2, δ_v must augment together with δ_T in order to hold the equality. Hence, the result is again equal to the one described above: ν and α assume larger values than reality, affecting the temperature distribution flow wise.

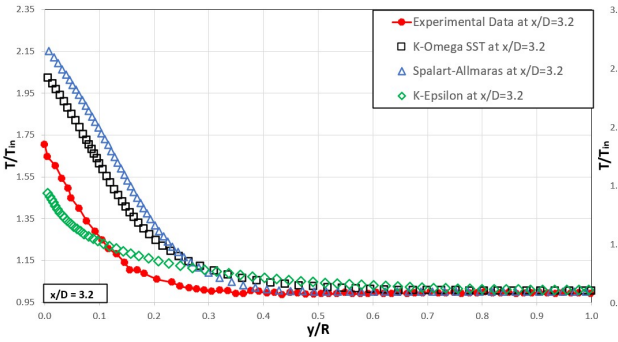

Figure 5.6: Comparison of RANS models and experimental data of normalised temperature field for 445 case at x/D = 3.2

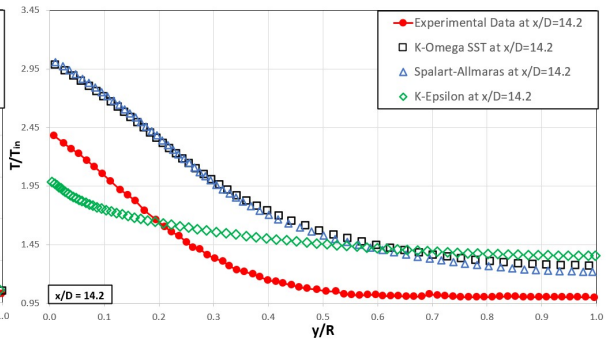

Figure 5.7: Comparison of RANS models and experimental data of normalised temperature field for 445 case at x/D = 14.2

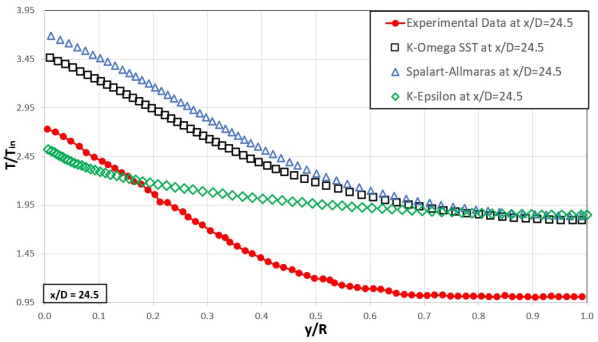

Figure 5.8: Comparison of RANS models and experimental data of normalised temperature field for 445 case at x/D = 24.5

Last case is the 635 shown in Fig. 5.9, Fig. 5.10 and Fig. 5.11, which is the most severe case with slightly bigger heat flux than 445 but Reynolds number equal to the 618 one.
Once more, the simulated thermal boundary layer develops quicker than the real experiments. Moreover, looking at Fig. 5.9 and Fig. 5.10, its increment is clearly steeper compared to the smooth development of the flow described by experimental result.

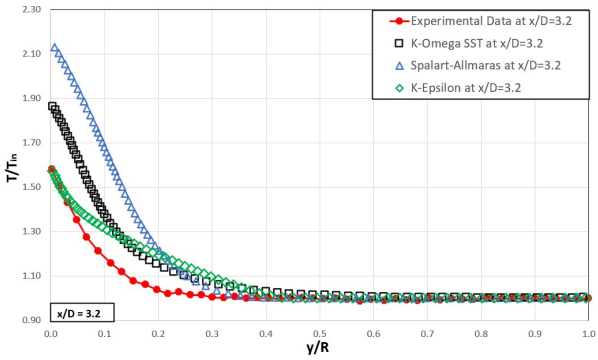

Figure 5.9: Comparison of RANS models and experimental data of normalised temperature field for 635 case at x/D = 3.2

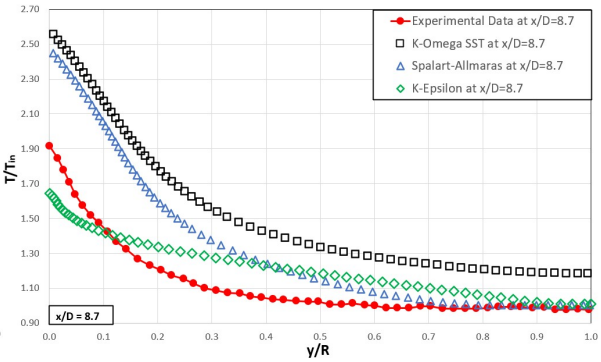

Figure 5.10: Comparison of RANS models and experimental data of normalised temperature field for 635 case at x/D = 8.7

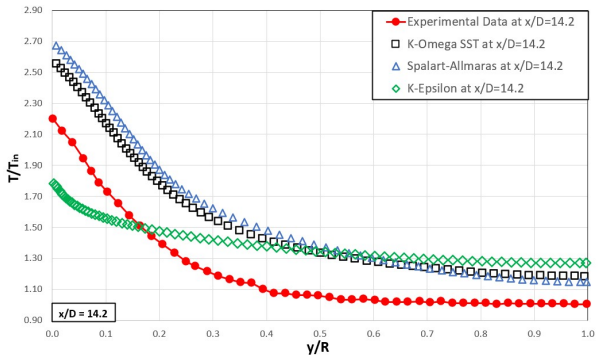

Figure 5.11: Comparison of RANS models and experimental data of normalised temperature field for 635 case at x/D = 14.2

Especially comparing $x/D = 3.2$ and $x/D = 8.7$, there is an addition of 30% temperature ratio for the k-ω SST (best performance) instead of a pick of 18 % at the wall in the real case.
In particular, the temperature tend to continuously increase even when the δ_T increment slows down. This can be noticed looking at data trend in Fig. 5.12 and Fig. 5.13, where the enlargement should be small even at $y/R = 0$, in contrast with any RANS simulation.

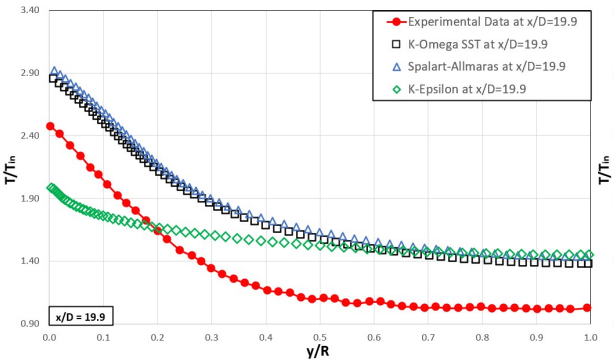

Figure 5.12: Comparison of RANS models and experimental data of normalised temperature field for 635 case at x/D = 19.9

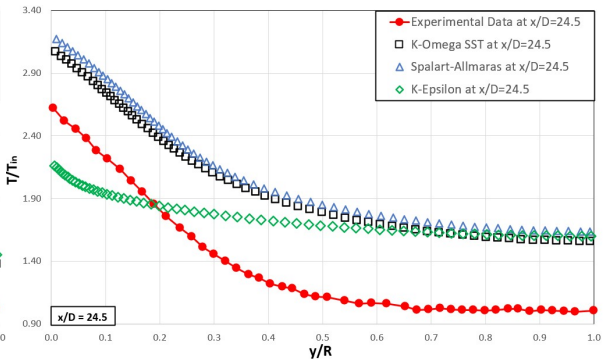

Figure 5.13: Comparison of RANS models and experimental data of normalised temperature field for 635 case at x/D = 24.5

In conclusion, the 3D set-up with LES model is necessary. The RANS modelled for wedge geometry is not useful to simulate turbulent heated pipe flows for three main reasons: the geometry together with RANS models are incapable to show vortex structure, underestimates the velocity field and at the same time over-estimates temperature values. Finally, the wrong temperatures influences the heat transfer process and fluid physical properties variations.

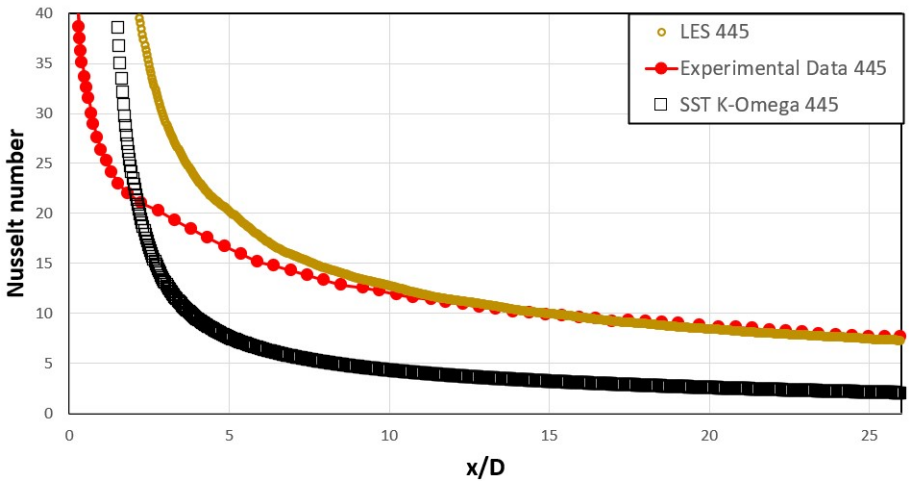

Figure 5.14: Comparison of axial Nusselt number variation between experimental data, RANS and LES for 445 case

Fig. 5.14 plots the Nusselt number along the axial coordinate of the pipe for the 445 case. The continuous decrease of the Nusselt number can be explained by its definition in Eq. 5.3.

$$Nu = \frac{h * D}{k} \tag{5.3}$$

The drop of the convective heat transfer coefficient (h) coincides with the reduction of the temperature difference between walls and fluid. At the same time the thermal conductivity (k) constantly rise.
Either 2D or 3D performs for $x/D \leq 9$ are not close to experimental data, then the LES perfectly get the Nusselt trend to stabilizes at constant number because of more uniform temperature distribution. In contrast, as expected the wedge plot is shifted down by a factor of 7 which consider an influence of viscosity and thermal boundary layer much more preponderant than reality.

5.3. LES Results

Fig. 5.15 gives the results for 445 case in three axial locations used also for the 2D results. This time, LES matches the flow behaviour at center pipe and better outcome next to the heating walls. At $x/D = 3.2$, the δ_T is already equal to 30 % of the radius and the error reaches its pick $y/R = 0.1$ (15 %).
At $x/D = 14.2$ the undervaluation is in the range of $0.2 < y/R < 0.45$ with a maximum of 13 %. The zone moved towards the pipe axis due to the fact that δ_T has grown, reaching half of the radius length [3].
Finally, at the end of the pipe ($x/D = 24.5$), the profile closely coincides with the experimental data with a very small 5 % difference in the worst case. However, the LES still has a wavy trend, much less pronounces than previous upstream data-set, instead of the parabola which is the sign of a fully developed thermal boundary layer [55].

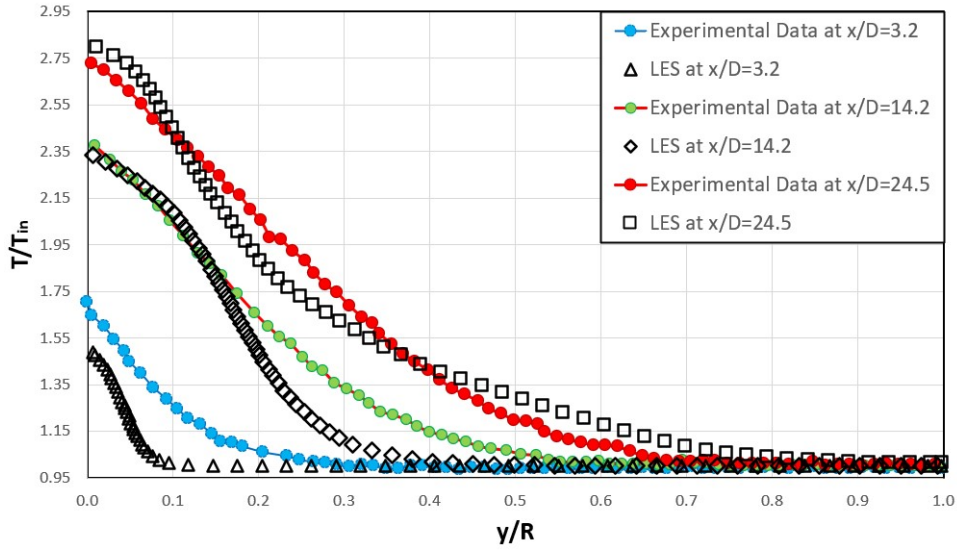

Figure 5.15: Comparison of LES model and experimental data of normalised temperature field for 445 case at x/D = 3.2, 14.2 and 24.5

This behaviour might be affected by the coarse calculations of the Boussinesq approximation. Nevertheless, lowing the heat flux such as in the 618 case, the simulation not only is more precise but also the critical region is reduce where the Kolomogorov scale is applied ($y/r \leq 0.1$) [23]. Indeed, from Fig. 5.16 it can be noticed a much smaller thermal boundary layer, which occupies basically half of the pipe radius comparing the same axial locations of 445 case.

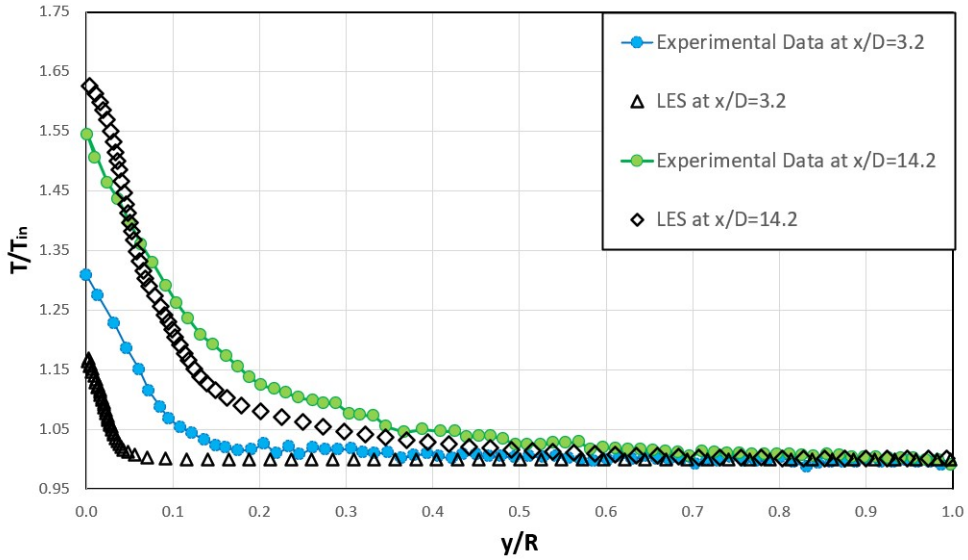

Figure 5.16: Comparison of LES model and experimental data of normalised temperature field for 618 case at x/D = 3.2 and 14.2

Moreover, a reduction of the error margin occurs already at $x/D = 3.2$ by 5 % and then by 8 % at $x/D = 14.2$. Especially the latter shows a complete turbulent profile because of the typical crushed parabola with a very steep trend close to the wall caused by large temperature gradients and a flat line at the center due to the high mixing of fluid portions [48].
Since the thermal boundary layer has reached the fully turbulent stage, Fig. 5.17 shows a plot line at $x/D = 24.5$ equal to the one at $x/D = 14.2$, just translated along the vertical axis because of an higher bulk temperature [3].

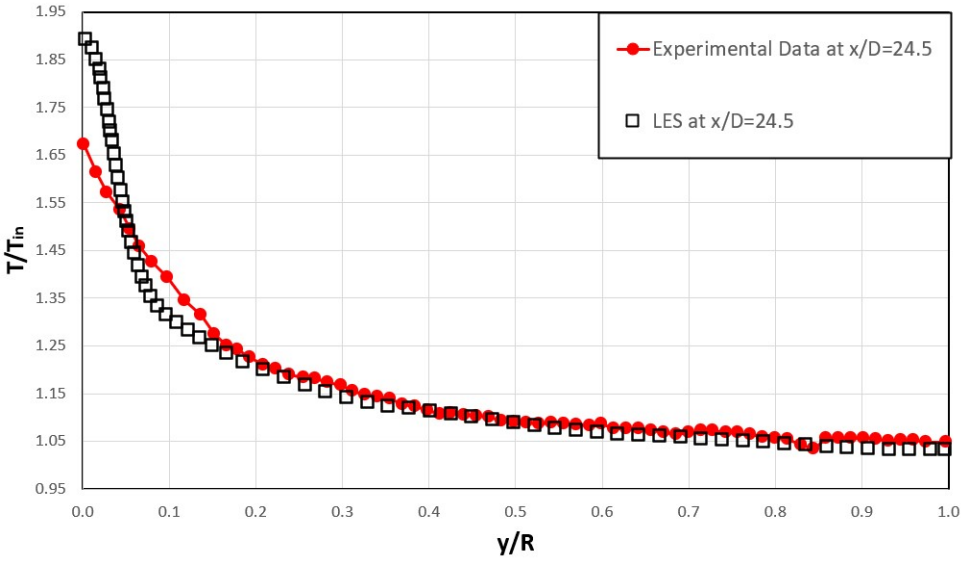

Figure 5.17: Comparison of LES model and experimental data of normalised temperature field for 618 case at x/D = 24.5

In Fig. 5.17, results are consistent for values at $y/R \geq 0.05$, next an acceptable and small overestimation around 10 % occurs.
The most turbulent case is the 635 because of high heat flux and Reynolds number. The strong inertia affects the thermal boundary layer which develops more slowly, occupying a portion of a radius comparable to 618 but with much higher wall temperatures due to larger heat flux. Looking at Fig. 5.18, upstream the model performs the best compared with the previous two simulations (9 % maximum at $x/D = 3.2$), then as before it cannot catch perfectly temperature grading. Still, the overestimation scores an acceptable 10 %.

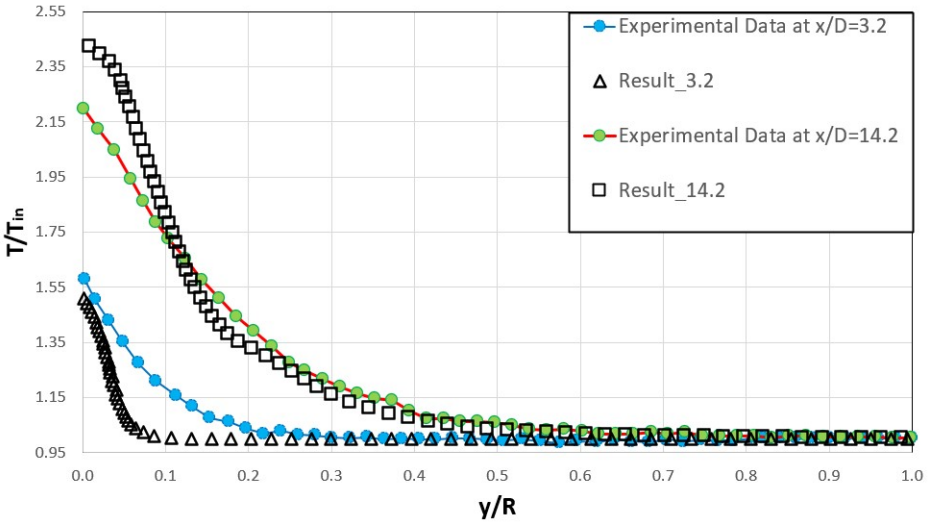

Figure 5.18: Comparison of LES model and experimental data of normalised temperature field for 635 case at x/D = 3.2 and 14.2

Moving downstream, the parabola appears again, but already at $x/D = 19.9$, before previous cases. The difference of T/T_{in} between simulation and reality is the same as 14.2, which means that it has reached its maximum becoming constant. However, the model suffers for solving the core flow at which T/T_{in} flattens as soon as $y \rightarrow R$. This is why from Fig. 5.19 it can be seen the line slightly above the experimental data interpolation.

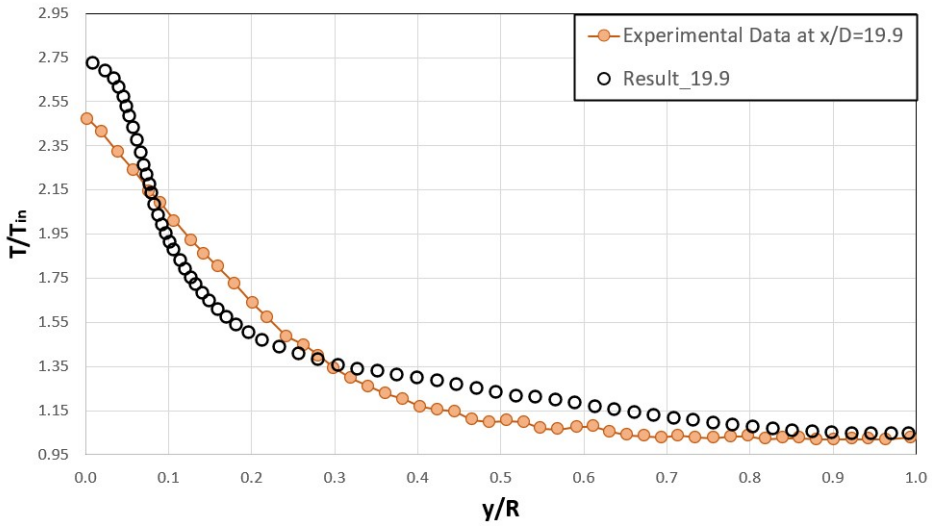

Figure 5.19: Comparison of LES model and experimental data of normalised temperature field for 635 case at x/D = 19.9

Overall the simulation gives satisfying outcomes because it can properly solve vortex structure and decent approximations at the wall. Concerning temperatures, it underestimates them at the pipe entrance for all the three cases, then it maintains a passable 10 % error range in the fully developed turbulent flow. The trend is summarised by Fig. 5.17, which visualises the temperature walls normalised by the inlet temperature along the pipe length.

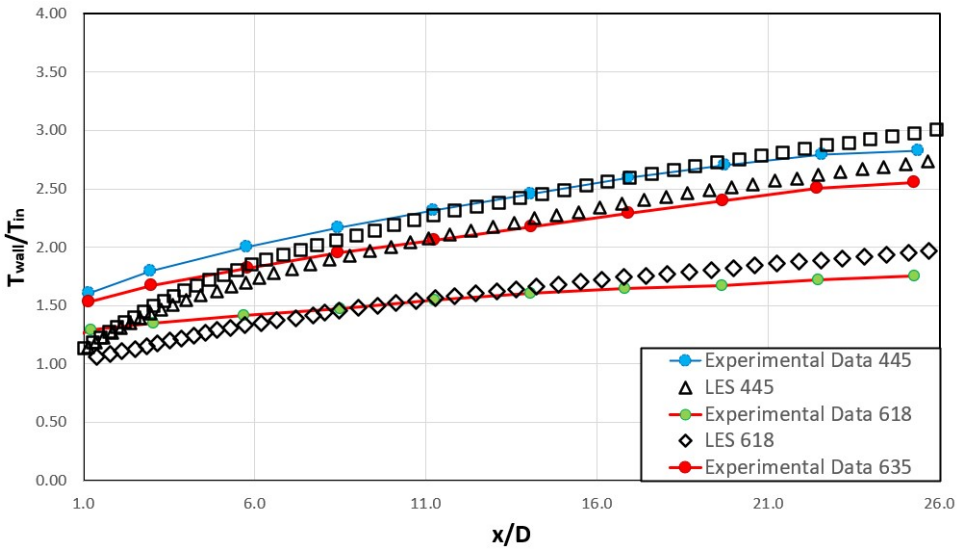

Figure 5.20: Comparison of three cases simulated by LES model and real experimental data of normalised temperature field along the entire axial pipe length

As described before, the wall gradients are usually underestimated at the beginning. This might happen because only the heated geometry is simulated, without considering the pipe part where the inertia acts already in the mixing phenomena [3]. Next, all the three simulations passing $x/D = 6$ gives tangential trends to experimental lines until the very end of the pipe where they start to diverge. Again, the difference might be caused by the zero gradient boundary condition which in reality should be an exhausted flow in atmospheric environment.

5.4. Role of Gravity

Fig. 5 21 clearly demonstrates how gravity strongly affects the flow in pipe applications. The absence of gravity causes a more uniform velocity field and basically a null acceleration of the flow towards the pipe exit.

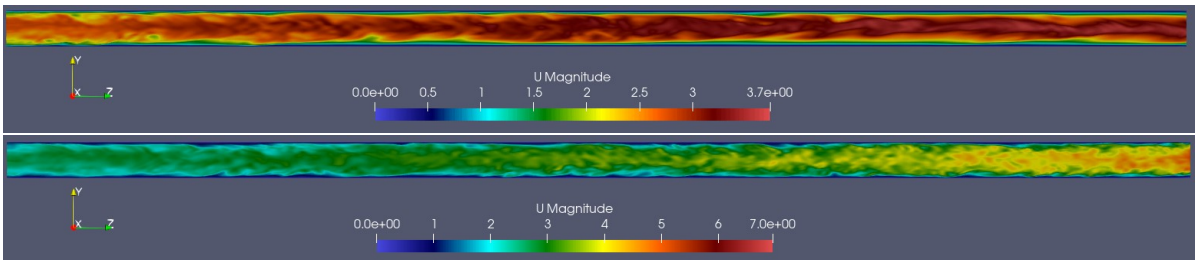

Figure 5.21: Velocity contours of the 618 case. From top to bottom: 3D LES WALE without gravity and 3D with LES WALE with gravity

Considering the contours given by Fig. 5.22, the wall temperatures are much higher than with gravity cases. The differentiation is lead by the gravity effects: boundary layer is thicker in case of absence of gravitational acceleration, suggesting that heat transfer coefficient will be also larger than mixed convection flow. Again, like last section the 618 behaviour is studied through T/T_{in} tendency across the radius.

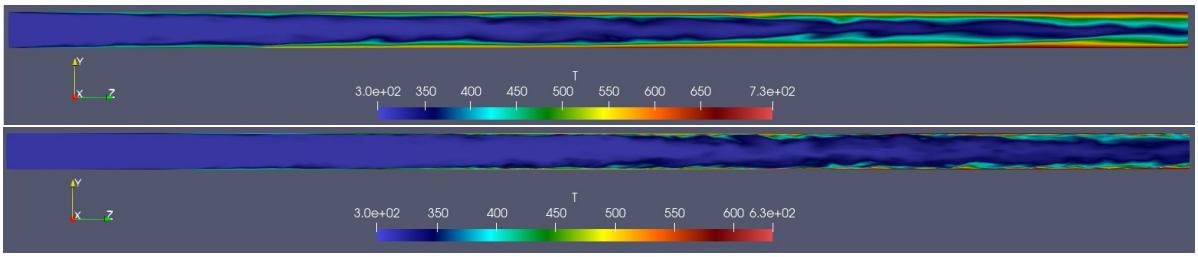

Figure 5.22: Temperature contours of the 618 case. From top to bottom: 3D LES WALE without gravity and 3D with LES WALE with gravity

Making a comparison between gravity and no gravity at $x/D = 3.2$ in Fig. 5.23, the gradient is incredibly higher. As a result, there is steeper trend and the δ_T occupies a 10 % more of the radius than the case with gravity.

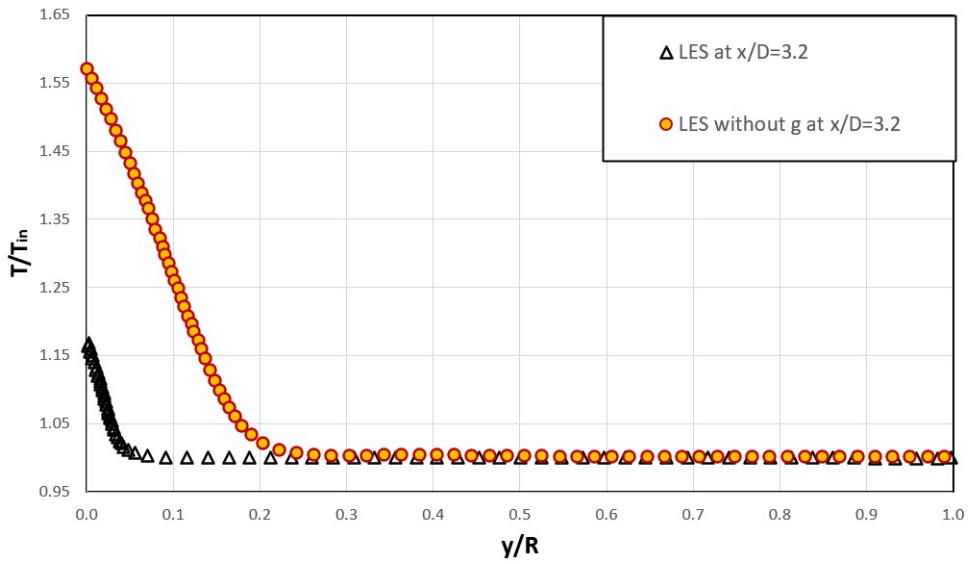

Figure 5.23: Comparison of LES model without gravity and experimental data of normalised temperature field for 618 case at x/D = 3.2

At $x/D = 14.2$ the case without gravity already resembles a parabola. The increment jump between wall and axis temperatures is much larger then the simulation with gravity. However, surprisingly the δ_T of the two scenarios has a comparable size.

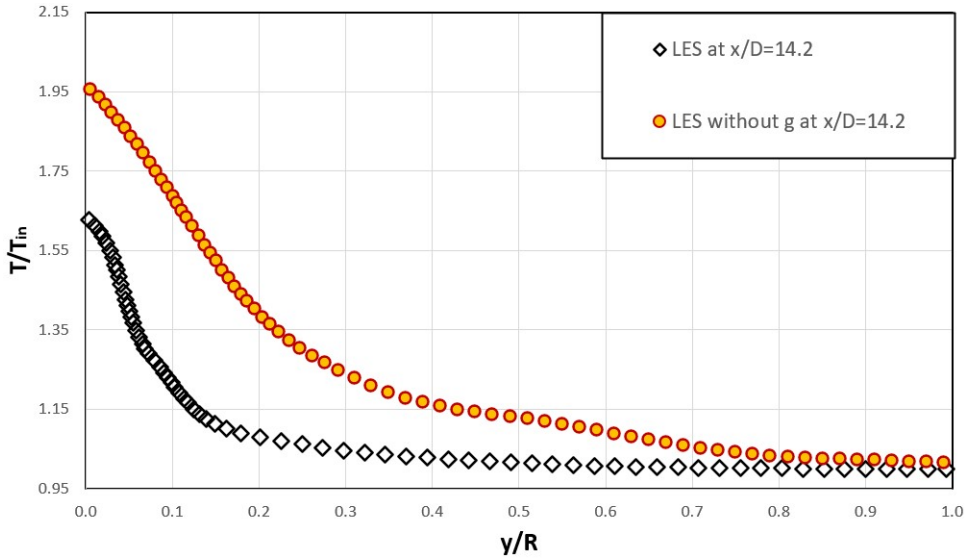

Figure 5.24: Comparison of LES model without gravity and experimental data of normalised temperature field for 618 case at x/D = 14.2

Lastly, the thermal boundary layer is fully developed at $x/D = 24.5$, but the LES simulation gives a rising linear trend from $y/R \leq 0.6$ and the center normalised temperature are slightly higher.
It implies that conduction has the leading role even in fully turbulent flow, causing a larger viscosity change in the flow, creating a stronger mixing process in the center which will not flatten the plot tendency.

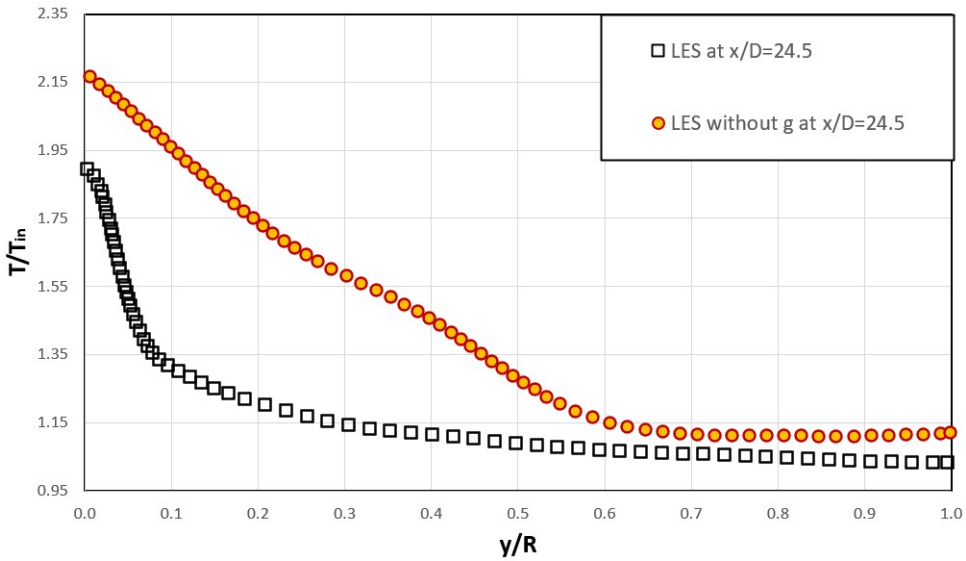

Figure 5.25: Comparison of LES model without gravity and experimental data of normalised temperature field for 618 case at x/D = 24.5

The physical behaviour can be better explained through Fig. 5.26 and recalling the definition of Nusselt number given with Eq. 5.3.

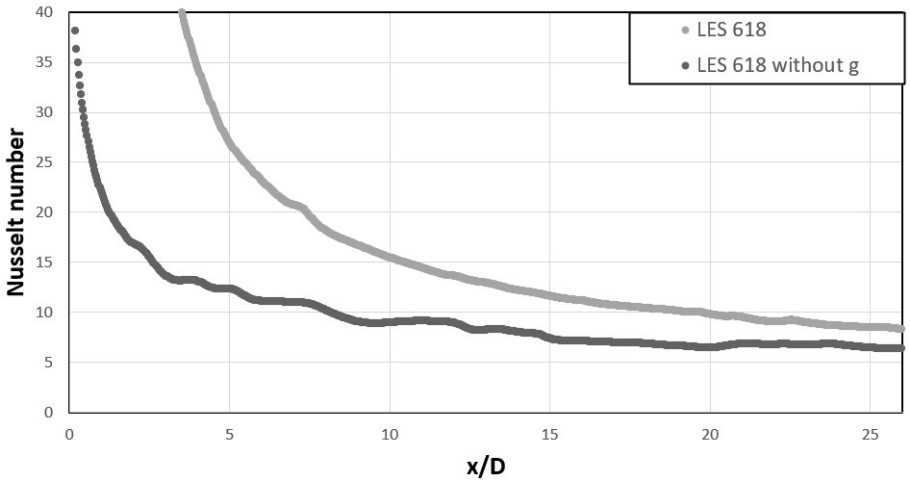

Figure 5.26: Comparison of axial Nusselt number variation between experimental LES for 618 case

According to Nuseelt definition, the ratio between convective heat transfer coefficient and thermal conductivity is lower than the case with gravity since the beginning. In addition, going downstream the boundary layer increases due to conductive heat transfer. In contrast this does not happen for convection so the ratio become smaller in the axial direction. To conclude the Nusselt number plot is below the gravity case everywhere.
Another important outcome is the visualization of the laminarization behaviour, which occurs in the 445 case due to gravity. Laminarization is a physical phenomena that links buoyancy and inertia effects [74], causing a transformation from a chaotic turbulent to laminar flow, as demonstrated in Fig. 5.27.

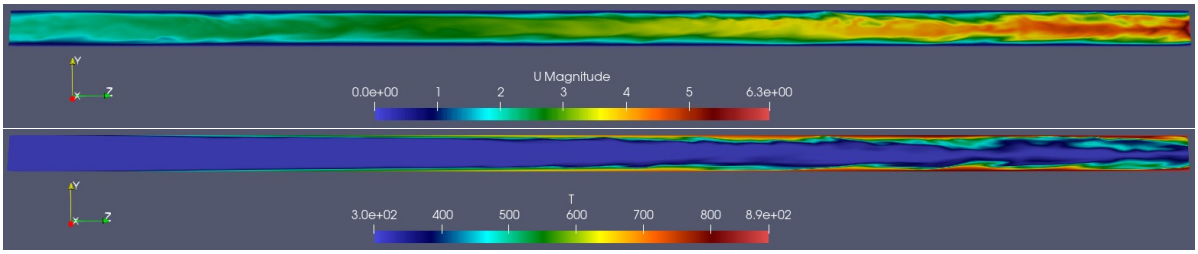

Figure 5.27: Velocity and temperature contours of the 445 case, where laminarization occurs

The velocity contours exhibit the typical boundary layer development of a laminarizing flow: it starts with small perturbations to then become smoother approximately at half pipe length and it ends transition to turbulent stage again.
The bottom figure shows the temperature field, where the boundary layer slowly thickens towards the exit. Again, as observed for velocity, the thermal boundary layer is basically laminar for almost three-quarters of pipe length, only close to the outlet turbulence is substantially visible.

6

Conclusion

The three studied cases have given the opportunity to look at different scenarios in order to answer the research questions listed in the introduction. The conclsions of thesis objectives are the following:

1. ***Does a 2D RANS simulation properly approximate a mixed convection turbulent pipe flow?***

   The RANS simulations modelled for the 2D geometry have performed poorly for all the scenarios. The best approximations are made by the $k-\omega$ SST; still, the computed error is too large to be acceptable. However, from a qualitative point of view, they are able to catch the thermal acceleration and the flow development.
   The RANS velocity field underestimates the experimental data, providing very large eddy viscosity values compared to reality. This is a result of a wrong translation of gravity effects from the model, which follows a rise of viscosity.
   Equal thoughts can be applied for the temperature field. The boundary layer development is too fast compared to the experimental data, resulting in an overestimation of normalised temperature since the beginning of the pipe. Indeed, the temperatures are incredibly high both at the walls and core flow. Especially the latter is due to the high mixing caused by the thick thermal boundary layer. Furthermore, the rate of the boundary layer development is proportional to wall heat flux and inversely correlated to the Reynolds number. This is the reason why the worst case is the 445 model.

2. ***How accurate is a 3D LES simulation, comparing it with real experimental data?***

   Undoubtedly, the results coming from the LES methodology, using WALE model, catches temperature gradients better than any RANS simulation discussed before. The velocity contours highlights a more pronounced thermal acceleration and shows the large scale vortex structure at the core flow. The boundary layer thickness grows slower, probably because LES catches the buoyancy forces.
   Moreover, normalised temperature trends are in general steeper and core flow matches almost perfectly with reality. The critical region is close to the wall, where an temperature calculation error occurs for $x/D \leq 0.3$. Nevertheless, wall approximations improve with the boundary layer development. This implies that for $y/r \leq 9$, the outcome is less precise, hitting an normalised temperature error pick of 15 % in the 445 case.

3. ***What are the main consequences of buoyancy concerning heat transfer?***

   It has been demonstrated how gravity strongly affects the flow field, using the 618 case. In fact, the absence of gravitational forces leads to a more uniform velocity field and thicker thermal boundary layer, guided by conduction heat transfer. This phenomena delivers larger temperature gradients at the heated walls, which in turns make the T/T_{in} dramatically steeper. In addition, the Nusselt number suffers from a substantial drop because of elevated thermal conductivity values, strictly connected to

the wide turbulent boundary layer.
In conclusion, gravity might generate laminarization as in 445 case. The contour plots illustrate a visual proof of a drastic change from chaotic turbulence to a close ordered laminar flow. The laminarization influences the velocity boundary layer, which is characterised by perturbations at the beginning, followed by a transition to smoothly laminar shape and ends in almost turbulent stage again. Similar considerations are provided for the temperature field, which mainly has a laminar boundary layer, disturbed by distinctive turbulence perturbations exclusively near by pipe exit.

7

Recommendations

Research objectives gained through this thesis might be an added value for understanding mixed convection. Still, there are many important fields and improvement that can be suggested for future studies:

- Comparing compressible LES model with the Boussinesq approximation, in order to understand if the rise of simulation complexity overweight the acquired accuracy.
- Simulate the same geometry with higher Reynolds numbers, assessing the effect of buoyancy in faster and more turbulent flows.
- Assess the different boundary layer development for same Reynolds number but different range of wall heat fluxes
- Create a LES or hybrid solver able to wall predict laminarization phenomena

Appendices

A

Code

A.1. Viscosity Model

The base of this new function is the "powerLaw" viscosity model, which is then modified with a new equation, as shown in Fig. A.1 to create a personal library.

```
\*---------------------------------------------------------------------------*/

#include "tempdeppowerLaw.H"
#include "addToRunTimeSelectionTable.H"
#include "surfaceFields.H"

// * * * * * * * * * * * * * * * Static Data Members * * * * * * * * * * * * * * * //

namespace Foam
{
namespace viscosityModels
{
    defineTypeNameAndDebug(tempdeppowerLaw, 0);

    addToRunTimeSelectionTable
    (
        viscosityModel,
        tempdeppowerLaw,
        dictionary
    );
}
}

// * * * * * * * * * * * * * * Private Member Functions  * * * * * * * * * * * * * * //

Foam::tmp<Foam::volScalarField>
Foam::viscosityModels::tempdeppowerLaw::calcNu() const
{
const volScalarField& T= U_.mesh().lookupObject<volScalarField>("T");

    return
    (
     k1_*Foam::pow(T, n_.value() + scalar(5.0)) + k2_*Foam::pow(T, n_.value() + scalar(4.0)) + k3_*Foam::pow(T, n_.value() + scalar(3.0))
     + k4_*Foam::pow(T, n_.value() + scalar(2.0)) + k5_*Foam::pow(T, n_.value() + scalar(1.0)) + k6_*Foam::pow(T, n_.value()) + k7_
    );
}
```

Figure A.1: Viscosity function implemented as a new OpenFOAM library

The frame code lines represent the function given by CoolProp according to Fig. 4.2. Therefore, "k" factors are the constant of the polynomial function and "n" is equal to unity and it is used to reach the order of equation magnitude.
Furthermore, the variables "k" and "n" are specified in the "transportProperties" section, as written in the code showed by Fig. A.2.

```
// * * * * * * * * * * * * * * * * * * Constructors  * * * * * * * * * * * * * * * * * //

Foam::viscosityModels::tempdeppowerLaw::tempdeppowerLaw
(
    const word& name,
    const dictionary& viscosityProperties,
    const volVectorField& U,
    const surfaceScalarField& phi
)
:
    viscosityModel(name, viscosityProperties, U, phi),
    tempdeppowerLawCoeffs_(viscosityProperties.optionalSubDict(typeName + "Coeffs")),
    k1_(tempdeppowerLawCoeffs_.lookup("k1")),
    k2_(tempdeppowerLawCoeffs_.lookup("k2")),
    k3_(tempdeppowerLawCoeffs_.lookup("k3")),
    k4_(tempdeppowerLawCoeffs_.lookup("k4")),
    k5_(tempdeppowerLawCoeffs_.lookup("k5")),
    k6_(tempdeppowerLawCoeffs_.lookup("k6")),
    k7_(tempdeppowerLawCoeffs_.lookup("k7")),
    n_(tempdeppowerLawCoeffs_.lookup("n")),
```

Figure A.2: Viscosity polynomial coefficients implemented as a new OpenFOAM library, imposed in "transportProperties" folder

A.2. Thermal Conductivity Function

Thermal conductivity is a flow field created by modifying the original solver "buoyantBoussinesqPimpleFoam". This is made by adding the new scalar field at "createFields.H" file (Fig. A.3).

```
Info<< "Reading field kappaLam\n" << endl;
volScalarField kappaLam
(
    IOobject
    (
        "kappaLam",
        runTime.timeName(),
        mesh,
        IOobject::NO_READ,
        IOobject::AUTO_WRITE
    ),
    mesh
);
```

Figure A.3: Creation of new field for thermal conductivity in "createFields.H"

Then a new file called "kappaEqn.H" is created for imposing the calculator to solve the polynomial function.

```
kappaLam = kappa1*Foam::pow(one*T, scalar(6.0))
      + kappa2*Foam::pow(one*T, scalar(5.0))
      + kappa3*Foam::pow(one*T, scalar(4.0))
      + kappa4*Foam::pow(one*T, scalar(3.0))
      + kappa5*Foam::pow(one*T, scalar(2.0))
      + kappa6*(one*T)
      + kappa7;
```

Figure A.4: Creation of new equation for thermal conductivity

The term "one" is a constant equal to one and used to simplify the dimension specification of the coefficients and defined as shown by Fig. A.4.

```
const dimensionedScalar one
(
 "one",
 dimless/dimTemperature,
 scalar(1.0)
);
```

Figure A.5: Definition of one constant

Again, the polynomial factors are read in the "transportProperties" section as seen in Fig. A.5.

```
dimensionedScalar kappa1
(
    "kappa1",
    //dimless,
    (dimLength*dimMass)/(dimTemperature*dimTime*dimTime*dimTime),
    laminarTransport
);

dimensionedScalar kappa2
(
    "kappa2",
    //dimless,
    (dimLength*dimMass)/(dimTemperature*dimTime*dimTime*dimTime),
    laminarTransport
);

dimensionedScalar kappa3
(
    "kappa3",
    //dimless,
    (dimLength*dimMass)/(dimTemperature*dimTime*dimTime*dimTime),
    laminarTransport
);

dimensionedScalar kappa4
(
    "kappa4",
    //dimless,
    (dimLength*dimMass)/(dimTemperature*dimTime*dimTime*dimTime),
    laminarTransport
);

dimensionedScalar kappa5
(
    "kappa5",
    //dimless,
    (dimLength*dimMass)/(dimTemperature*dimTime*dimTime*dimTime),
    laminarTransport
);

dimensionedScalar kappa6
(
    "kappa6",
    //dimless,
    (dimLength*dimMass)/(dimTemperature*dimTime*dimTime*dimTime),
    laminarTransport
);
dimensionedScalar kappa7
(
    "kappa7",
    //dimless,
    (dimLength*dimMass)/(dimTemperature*dimTime*dimTime*dimTime),
    laminarTransport
);
```

Figure A.6: Thermal conductivity polynomial coefficients, imposed in "transportProperties" folder

A.3. Heat Flux Boundary Condition

In OpenFOAM, values at the boundaries are found through this generic equation [63]:

$$X_B = f_{ref} + (1-f)\left[X_x + \frac{Grad_{ref}(X)}{deltaCoeffs}\right] \tag{A.1}$$

where X_{ref} is the reference value at the boundary, X_x is the quantity of the value at the cell center, $Grad_{ref}(X)$ is the reference gradient of the variable, $deltaCoeffs$ is the inverse of the distance between the face center and the cell center ($deltaCoeffs = 1/\delta$) and f a weighted factor that defines the boundary condition type:

$$\begin{cases} \text{f} = 1 & \Longrightarrow \textit{Dirichlet boundary condition} \\ \text{f} = 0 & \Longrightarrow \textit{Neumann boundary condition} \\ 0 < \text{f} < 1 & \Longrightarrow \textit{Robin boundary condition} \end{cases} \tag{A.2}$$

This equation must be written in function of temperature. Therefore, looking at Fig. A.7 it is possible to extrapolate the wall temperature through the energy balance.

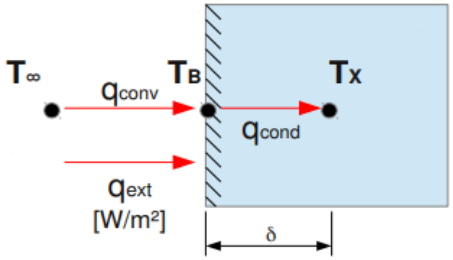

Figure A.7: Schematic drawing of the heat balance at the pipe wall

Balancing the heat fluxes:

$$q_{conv} + q_{ext} = q_{cond} \tag{A.3}$$

$$\begin{cases} q_{conv}/A = h \cdot (T_\infty - T_B) \Longrightarrow \textit{Convective heat transfer} \\ q_{conv}/A = \frac{k}{\delta} \cdot (T_B - T_X) \Longrightarrow \textit{Conduction heat transfer} \end{cases} \tag{A.4}$$

where A corresponds to Area, which in case of a cell analysis is actually δ.
Now Eq. A.3 can be re-equated as:

$$T_B = \frac{h}{\left(\frac{k}{\delta} + h\right)} T_\infty + \frac{\frac{k}{\delta}}{\left(\frac{k}{\delta} + h\right)} T_X + \frac{q_{ext}}{\left(\frac{k}{\delta} + h\right)} \tag{A.5}$$

Finally:

$$T_B = \frac{h}{\left(\frac{k}{\delta} + h\right)} T_\infty + \frac{\frac{k}{\delta}}{\left(\frac{k}{\delta} + h\right)} \left[\frac{T_X + q_{ext}}{\delta}\right] \tag{A.6}$$

Thus, Eq. A.6 has the same form of Eq. A.1, considering the following imposition:

$$f = \frac{1}{1 + \frac{k}{h\delta}} \tag{A.7}$$

$$1 - f = \frac{\frac{k}{\delta}}{1 + \frac{k}{h\delta}} \tag{A.8}$$

Based on the equation, the Fig. A.7 shows how the coded has been developed.

```
Pipe
{
    type codedMixed;
    refValue uniform 300;           //default value
    refGradient uniform 0;          //default value
    valueFraction uniform 0;
    redirectType HeatFlux_BC;       //name of new BC type

    code
    #{
            const scalar q = 4242.147418;
            const scalarField& kwall = patch().lookupPatchField<volScalarField, scalar>("kappaLam");       //extracting thermal conductivity at boundary
            this->refValue() = 0;                                                                          //Wall temperature
            this->refGrad() = q/kwall;                                                                     //dT/dx = -h(Tboundary - Tamb)/conductivity
            this->valueFraction() = Zero;
    #};

    codeInclude
    #{
            #include "interpolationTable.H"
            #include "IFstream.H"
            #include "OFstream.H"
    #};

    codeOptions
    #{
            -I$(LIB_SRC)/finiteVolume/lnInclude
    #};
}
```

Figure A.8: CodedMixed boundary condition for the wall

A.4. Velocity Inlet

The velocity inlet is based on Eq. 4.53 and the coordination system employed for mesh construction.

```
\*---------------------------------------------------------------------------*/
FoamFile
{
    version     2.0;
    format      ascii;
    class       volVectorField;
    object      U;
}
// * * * * * * * * * * * * * * * * * * * * * * * * * * * * * * * * * * * * * //

dimensions      [0 1 -1 0 0 0 0];

internalField   uniform (0 0 0);

boundaryField
{
    Inlet
    {
        type            codedFixedValue;
        value           uniform (3.46 0 0);

        name            parabolicProfile;
        code
        #{
                const vectorField& Cf = patch().Cf();
                vectorField& field = *this;

                const scalar c =  0;
                //const scalar c1 = 0;
                const scalar r =  0.0137;
                const scalar Umax = 3.46;
                const scalar Npow  = 5.5;

                forAll(Cf, faceI)
                {
                        const scalar z = Cf[faceI][2];
                        const scalar y = Cf[faceI][1];
                        const scalar radius = mag(y); //pow((y-c)*(y-c)+(z-c1)*(z-c1), 0.5);

                        field[faceI] = vector(Umax*(1-pow((radius/r), Npow)), 0, 0);
                }
    #};
    }
```

Figure A.9: Code of velocity parabola imposed as inlet for RANS simulations

Fig. A.9 shows that the origin of the axis is equal to the center of the inlet pipe. This is the reason why c and $c1$ are set to zero. Furthermore, the velocity component is imposed in flow direction (x) and the function is evaluated at the center of the cells.

Bibliography

[1] *Course of Modelling of Thermo- Hydrodynamic systems (ME45155).* 2018.

[2] A. Bontemps A. Bruch and S. Colasson. *Experimental investigation of heat transfer of supercritical carbon dioxide flowing in a cooled vertical tube.* Internal journal for heat and mass transfer, 2009.

[3] Donald M. McEligot A. Mohsen Shehata. *Mean structure in the viscous layer of strongly heated internal gas.* International Journal of Heat and Mass transfer.

[4] J. W. Ackerman. *Pseudoboiling heat transfer to supercritical pressure water in smooth and ribbed tubes.* Journal of Heat transfer.

[5] T. Aicher and H. Martin. *New correlations for mixed turbulent natural and forced convection heat transfer in vertical tubes.* Int. J. Heat Mass Transfer, 1997.

[6] G. Alfonsi. *Reynolds-Averaged Navier-Stokes Equations for Turbulence Modeling.* Applied Mechanics Reviews.

[7] Shehata AM. and McEligot DM. *Mean structure in the viscous layer of strongly-heated internal gas flows: measurements.* Int. J. Heat Mass Transf., 1998.

[8] Yoon Y. Bae. *A new formulation of variable turbulent Prandtl number for heat transfer to supercritical fluids.* Elsevier, International Journal of Heat and Mass Transfer, 2015.

[9] Choi H. Bae JH, Yoo JY. *Direct numerical simulation of turbulent supercritical flows with heat transfer.* Phys. Fluids 17, 2005.

[10] Ian H. Bell, Jorrit Wronski, Sylvain Quoilin, and Vincent Lemort. *Pure and Pseudo-pure Fluid Thermophysical Property Evaluation and the Open-Source Thermophysical Property Library CoolProp,* volume 53. 2014.

[11] J. Boussinesq. *Théorie de l'Ecoulement Tourbillant.* Mém. prés. Acad. Sci., Vol. XXIII.

[12] Baik S. Ahn Y. Cho S.K., Kim M. and Lee J. *Investigation of the bottoming cycle for high efficiency combined cycle gas turbine system with supercritical carbon dioxide power cycle.* ASME turbo expo 2015: turbine technical conference and exposition, 2015.

[13] J. Y. M. Poon D. B. T. Kenning, R. A. W. Shock. *Local reduction in heat transfer due to buoyancy effects in upward turbulent flow.* 5th International Heat Transfer Conference.

[14] Anil W. Date. *Introduction to Computational Fluid Dynamics.* Cambridge University Press.

[15] Eugene de Villiers. *The Potential of Large Eddy Simulation for the Modelling of Wall Bounded Flows.* Department of Mechanical Engineering, Imperial College London.

[16] Giorgio Noseda Duilio Citrini. *Idraulica.* Milano, ambrosiana.

[17] B.E. Launder e D.B. Spalding. *The numerical computation of turbulent flows.* Computer Methods in Applied Mechanics and Engineering.

[18] D. Mowla E. Sadatshojaei and D.A. Wood. *Review of progress in microalgal biotechnology applied to wastewater treatment in: Sustainable Green Chemical Process and their Allied Applications.* Springer Nature, 2020.

[19] D. Mowla E. Sadatshojaei and D.A. Wood. *Third generation of biofuels exploiting microalgae, in: Sustainable Green Chemical Process and their Allied Applications.* Springer Nature, 2020.

[20] Amir Faghri. *Review and Advances in Heat Pipe Science and Technology.* Journal of Heat transfer.

[21] J. Fewster. *Mixed convection and free convective heat transfer to supercritical pressure fluids flowing in vertical tubes.* PhD. Thesis, University of Manchester, 1976.

[22] Menter FR. *Zonal two equation k- turbulence models for aerodynamic flows.* Presented at Fluid Dyn. Conf. Orlando, 1993.

[23] Bendiks J. Boersma Frans T.M. Nieuwstadt and Jerry Westerweel. *Turbulence Introduction to Theory and Applications of Turbulent Flows.* Springer, 2016.

[24] H. L. Herring G. L. Mellor. *A Survey of the Mean Turbulent Field Closure Models.* AIAA Journals.

[25] OpenFoam User Guide. *https://www.openfoam.com/documentation/guides/latest/doc/guide-applications-solvers-pimple.html.* .

[26] OpenFoam User Guide. *https://www.openfoam.com/documentation/guides/latest/doc/guide-turbulence-ras-spalart-allmaras.html.* .

[27] OpenFoam User Guide. *https://www.openfoam.com/documentation/guides/latest/doc/guide-turbulence-les-wale.html.* .

[28] OpenFoam User Guide. *https://cfd.direct/openfoam/user-guide/v6-fvsolution/.* .

[29] OpenFoam User Guide. *https://www.openfoam.com/documentation/guides/latest/api/dir*$_6$64 $1f82fbb5cbac3ab878fd864868f3e.html$..

[30] OpenFoam User Guide. *https://www.openfoam.com/documentation/user-guide/a-reference/a.1-standard-solvers.* .

[31] OpenFoam User Guide. *https://www.openfoam.com/documentation/guides/latest/doc/guide-turbulence-ras-k-epsilon.html.* .

[32] OpenFoam User Guide. *https://www.openfoam.com/documentation/guides/latest/doc/guide-turbulence-ras-k-omega-sst.html.* .

[33] OpenFoam User Guide. *https://www.openfoam.com/documentation/guides/latest/doc/guide-solvers-under-relaxation.html.* .

[34] OpenFoam User Guide. *https://www.openfoam.com/documentation/guides/latest/doc/guide-schemes-time-backward.html.* .

[35] O.E. Adedeji Z. Chára C.A.R. Duarte V. Matoušek M.G. Rasteiro R.S. Sanders R.C. Silva F.J. de Souza G.V. Messa, Q. Yang. *Computational Fluid Dynamics Modelling of Liquid–Solid Slurry Flows in Pipelines: State-of-the-Art and Future Perspectives.* Blaž Likozar.

[36] K. M. Munisamy M. A. Wahid H. K. Dawood, H. A. Mohammed Nor Azwadi Che Sidik. *Forced, natural and mixed-convection heat transfer and fluid flow in annulus: A review.* Elsevier, International Communications in Heat and Mass Transfer.

[37] Bae JH. He S, Kim WS. *Assessment of performance of turbulence models in predicting supercritical pressure heat transfer in a vertical tube.* Int. J. Heat Mass Transf., 2008.

[38] P. Bradshaw J. B. Cazalbou. *Turbulent transport in wall-bounded flows, evaluation of model coefficients using Direct Numerical Simulation.* Physics of Fluids A: Fluid Dynamics 5.

[39] Davide Scarselli Nazmi Burak Budanur Michael Riedl Ashley P. Willis Marc Avila Björn Hof Jakob Kühnen, Baofang Song. *Destabilizing turbulence in pipe flow.* Nature Physics, Vol. 14.

[40] Jackson JD. *Consideration of the heat transfer properties of supercritical pressure water in connection with the cooling of advanced nuclear reactors.* Basin Nucl. Conf., 2002.

[41] Jackson JD. *Validation of an extended heat transfer equation for fluids at supercritical pressure.* Issy-les-Moulineaux, France: Gen. IV Int. Forum, 2009.

[42] Milovan Peric Joel H. Ferziger. *Computational Methods for Fluid Dynamics*. Springer.

[43] Kim Y.I. Bae Y.Y. Cho B.H. Kim, S.H. *Numerical simulation of the vertical upward flow of water in a heated tube at supercritical pressure*. N. Proc. ICAPP, 2004.

[44] Kim B. Kim M.S., Ahn Y. and Lee JI. *Study on the supercritical CO2 power cycles for landfill gas firing gas turbine bottoming cycle*. Elsevier, 2016.

[45] Fefelova ND. Krasyakova LY, Belyakov II. *Hydraulic resistance with isothermal and non isothermal flow of the medium at supercritical pressure*. Therm. Eng., 1973.

[46] LearnCAX. *https://www.learncax.com/knowledge-base/blog/by-category/cfd/basics-of-y-plus-boundary-layer-and-wall-function-in-turbulent-flows*.

[47] L. Mahrt. *Encyclopedia of Atmospheric Sciences*. Academic Press.

[48] A. F. Mills. *Basic Heat and Mass Transfer*. Pearson.

[49] Zefei Zhu M.Mizanur Rahman, L. V. Ming. *Impact of Prandtl numbers on turbulence modeling*. The Second International Conference on Physics, Mathematics and Statistics.

[50] O.Schmidt M.Sommerfeld M.Weickert, G.Teike. *Investigation of the LES WALE turbulence model within the lattice Boltzmann framework*. Computers Mathematics with Applications Volume 59, Issue 7.

[51] F. Nicoud and F. Ducros. *Subgrid-scale stress modelling based on the square of the velocity gradient tensor*. Flow Turbulence and Combustion.

[52] U.S. Department of Energy. *THERMODYNAMICS, HEAT TRANSFER, AND FLUID FLOW. DOE Fundamentals Handbook*.

[53] S. R. Allmaras P. R. Spalart. *A one-equation turbulence model for aerodynamic flows*. La Recherche Aerospatiale.

[54] Polyakov AF. Petukhov BS. *Heat Transfer in Turbulent Mixed Convection*. ed. BE Launder. New York: Hemisphere, 1988.

[55] David R. Dowling Pijush K. Kundu, Ira M. Cohen. *Fluid Mechanics*. Academic Press.

[56] Duffey R.B. Pioro I.L. and Dumouchel T.J. *Hydraulic resistance of fluids flowing in channels at supercritical pressures (survey)*. Nucl. Eng. Des., 2004.

[57] Maria Giovanna Tanda Sandro Longo. *Esercizi di Idraulica e di Meccanica dei Fluidi*. Springer.

[58] M. E. Shitsman. *Natural convection effect on heat transfer to a turbulent water flow in intensively heated tubes at supercritical pressures*. Institution of Mechanical Engineers.

[59] A. A. Steiner. *On the reverse transition of a turbulent flow under the action of buoyancy forces*. Journal of Fluid Mechanics.

[60] Jaroslav Stigler. *ANALYTICAL VELOCITY PROFILE IN TUBE FOR LAMINAR AND TURBULENT FLOW*. 18th International Conference ENGINEERING MECHANICS.

[61] Hirata M. Tanaka H., Tsuge A. and Nishiwaki. *Effects of buoyancy and of acceleration owing to thermal expansion on forced turbulent convection in vertical circular tubes—criteria of the effects, velocity and temperature profiles, and reverse transition from turbulent to laminar flow*. Int. J. Heat Mass Transf., 1973.

[62] Leont'ev AI. Tarasova NV. *Hydraulic resistance during flow of water in heated pipes at supercritical pressures*. High Temp., 1968.

[63] Foaming Time. *https://foamingtime.wordpress.com/l*.

[64] K.D. Squired T.S. Lund, X.H. Wu. *Generation of turbulent inflow data for spatially-developing boundary layer simulations*. Journal Computational Physics, Vol. 140, No. 2, pp. 233–258.

[65] Kurganov V.A. and Kaptil'ny A.G. *Velocity and enthalpy fields and eddy diffusivities in a heated supercritical fluid flow.* Exp. Therm. Fluid Sci., 1992.

[66] H K Versteeg and W Malalasekera. *An Introduction to Computational Fluid Dynamics.* Pearson, 1995.

[67] B. E. Launder W. P. Jones. *The calculation of low-Reynolds number phenomena with a two-equation model of turbulence.* International Journal of Heat Mass Transfer.

[68] Wikipedia. *https://en.wikipedia.org/wiki/Thermal$_e xpansion$*.

[69] D. Williams. *Extraction with supercritical gases.* Chem. Eng. Sci. 36 (11), 1981.

[70] CFD with a mission. *https://caefn.com/openfoam/wale-sgs-model.* .

[71] CFD with a mission. *https://caefn.com/tag/buoyantboussinesqpimplefoam.* .

[72] Tsujikawa Y. and Northam G.B. *Effects of hydrogen active cooling on scramjet engine performance.* Int. J. Hydrogen Energy, 1996.

[73] Ishiwatari Y. Liu J. Yang J., Oka Y. and Yoo J. *A numerical investigation of heat transfer in upward flows of supercritical water in circular tubes and tight fuel rod bundles.* Nucl. Eng. Des., 2007.

[74] Jung Yul Yoo. *The Turbulent Flows of Supercritical Fluids with Heat Transfer.* Annual review of Fluid Mechanics, 2012.

[75] Choi H. You J, Yoo JY. *Direct numerical simulation of heated vertical air flows in fully developed turbulent mixed convection.* Int. J. Heat Mass Transf., 2003.

[76] L-K. Tseng Z. Dai and G.M. Faeth. *Velocity/mixture fraction statistics of round self preserving, buoyant turbulent flumes.* National Heat Transfer Conference-Volume 2, ASME, 1995.